Available online at www.sciencedirect.com

jmr&t Journal of Materials Research and Technology

journal homepage: www.elsevier.com/locate/jmrt

Change in the structure and mechanical properties of Al–Mg–Si alloys caused by the addition of other elements: A comprehensive review

Pallavi Singh [a], *D Atchuta Ramacharyulu* [b], *Nikhil Kumar* [a,*], *Kuldeep K. Saxena* [c], *Sayed M. Eldin* [d]

[a] School of Materials Science and Technology, Indian Institute of Technology (BHU), Varanasi 221005, India
[b] Department of Mechanical Engineering, Institute of Aeronautical Engineering, Hyderabad Telangana, India
[c] Division of Research and Development, Lovely Professional University, Phagwara 144411, India
[d] Center of Research, Faculty of Engineering, Future University in Egypt New Cairo 11835, Egypt

ARTICLE INFO

Article history:
Received 7 August 2023
Accepted 21 September 2023
Available online 5 October 2023

Keywords:
Al–Mg–Si alloy
Heat-treatment
Artificial ageing
Natural ageing
Room temperature
Guinier preston zone

ABSTRACT

Understanding 6xxx AA (Al–Mg–Si alloys) relies heavily on structural analysis at the atomic level. Because the nanoscale precipitates that form during artificial ageing essentially strengthen the alloys, it is crucial to lessen the negative effects of Natural Ageing (NA) and enhance the age hardening of Al–Mg–Si alloys. Numerous studies have shown that when different elements are added to 6xxx AA, NA is suppressed. This work includes a thorough and numerical description of the various elements that are added to 6xxx AA. This article gives information on the additional elements Li, Cu, Zn, and Ag that will form new phases and occupy a preferred site in 6xxx AA at different weight percentages. However, between metastable phases, 6xxx AA exhibit different element segregation, which improved the mechanical properties like hardness reported in this review work. Additionally, research on the addition of various other elements, such as Ni, Co, Au, and Cd to 6xxx AA is reported in this review paper to summarise the influence of these elements on the evolution of microstructural features and their correlation with mechanical properties. This area has received very little research and may be used in the future to enhance the mechanical properties of 6xxx AA. By encouraging precipitate nucleation, morphology, and mechanical properties through the addition of foreign elements, the results of this review paper reveal a novel pathway for precipitation hardening.

1. Introduction

The need to reduce CO_2 emissions is more urgent as climate change's effects the economy, society, industry, and environment become a major issue [1]. To stop environmental deterioration and advance sustainable development, industries everywhere are putting an emphasis on implementing environmental, social, and governance management. To become carbon neutral, the automotive industry, which is the main producer of CO_2 emissions, is developing and converting

* Corresponding author.
E-mail addresses: nikhil.mst@itbhu.ac.in, nikhil.shishodiya@gmail.com (N. Kumar).
https://doi.org/10.1016/j.jmrt.2023.09.220

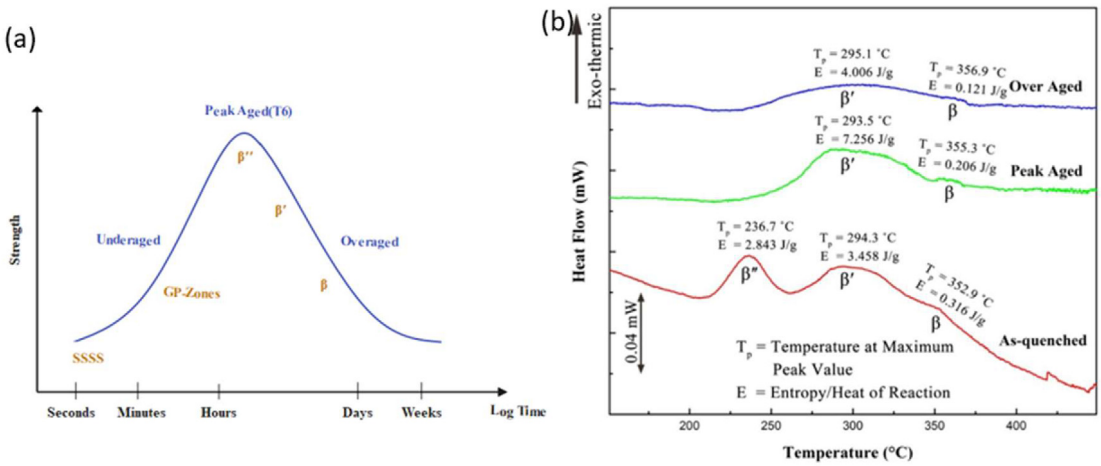

Fig. 1 – (a) Strength changes as an Al–Mg–Si alloy ages artificially. Data taken from Ref. [15], (b) DSC traces of A357 alloy under peak-aged, over-aged, and as-quenched conditions; all samples underwent an 8-h solution treatment. Adapted with permission from Ref. [20].

to low-emission automobiles. Nearly 36% of the nation's total CO_2 emission in 2020 came from the transport sector which is nearly 1630 million metric tonnes [2]. The best way to lower CO_2 emissions is to use the fuel which is having high efficiency, powerful performance and offer an environmentally friendly lightweight component. A vital lightweight material, hypoeutectic (12 wt.% Si) 6xxx AA have number of advantageous traits, such as a high strength-to-weight ratio, superior cast-ability, mechanical qualities, recyclability, good weldability and excellent corrosion resistance. As a result, it is widely used to make large casts with sophisticated structures for the transportation industry, including chassis frames and housings for battery module housings for electric cars [2,3]. Electric vehicle manufacturers needed lightweight materials to make the various parts of EVs (Electric Vehicles). 6xxx AA

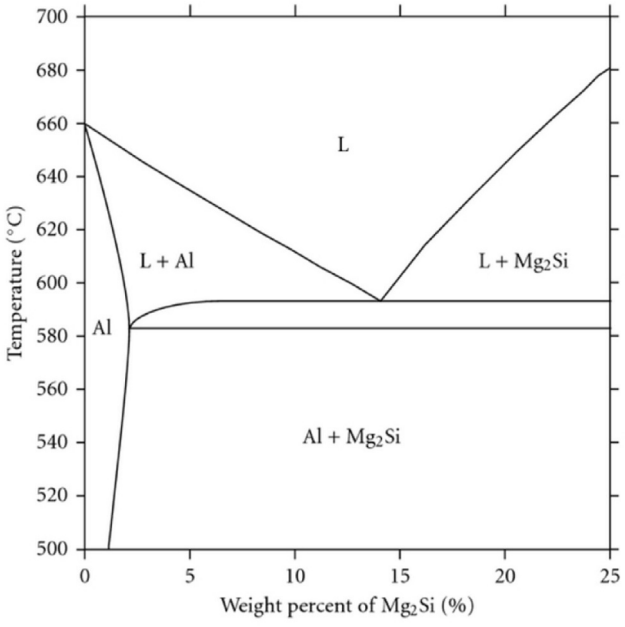

Fig. 2 – Aluminium (Al)-Magnesium silicide (Mg_2Si) phase diagram [22].

are more regularly employed to produce various EV components due to their high specific strength. The forged 6xxx AA component can replace steel-based components in EVs due to its lower density [3].

6xxx AA is the top choice for auto-body sheet materials. The nanoscale structural study is now possible, thanks to major advancements in analytical and computational materials characterisation technology. This has been demonstrated to be crucial for comprehending and developing aluminium alloys, especially the Al–Mg–Si system. It is now obvious that atomic-scale research into precipitate structures is required to provide alloys with the requisite macroscopic characteristics [4–9]. The development of nanoscale precipitate particles during ageing strengthens 6xxx aluminium alloys primarily. To enhance the mechanical qualities, it is essential to control the precipitate's distribution, orientation, size, and composition. Clusters, GP zones, β″, β′, U1, U2, B′ phases, phase, and Si particle were the order in which 6xxx AA precipitated [10–13]. Fig. 1 depicts the strength evolution of 6xxx-alloys with time [14,15]. Clusters with a disorganised configuration resulted from the fusion of Mg, Si, and their atoms. The $Mg_5Al_2Si_4$ stoichiometry and C2/*m* structure of the needle-like β″ structure. There are four phases that make up the ageing behaviour: β′ (Mg_9Si_5), U1 ($MgAl_2Si_2$), U2 ($Al_4Mg_4Si_4$), and B′ ($Al_3Mg_9Si_8$) [16–19] and their strength changes shown in Fig. 1(a). In the DSC curves of peak-aged and over-aged samples, the peak phases β" have disappeared compared to the as-quenched samples, implying that only β' and β precipitates form. This indicates precipitates were already present before the DSC testing due to the ageing treatment. The β' peaks in these DSC curves likely result from the transformation of previous β" peaks into β' during the DSC test heating, as illustrated in Fig. 1(b) [5].

In this class of alloys, the ratio of Mg to Si is roughly 1.73:1, with a maximum of 1.5% in each [21]. Mg_2Si is very soluble (1.8% solubility) in aluminium and becomes less soluble as temperature increases. Fig. 2 displays the Mg_2Si phase of 6xxx AA, which symbolises the solubility of Mg and Si as a function of temperature. In the 6xxx series, the Mg/Si solubility ratio is

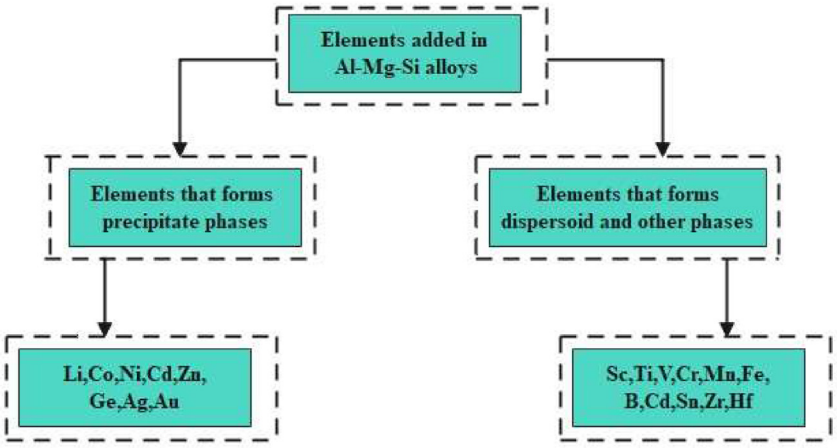

Fig. 3 – Elements forming precipitate and Dispersoids with Al–Mg–Si alloy.

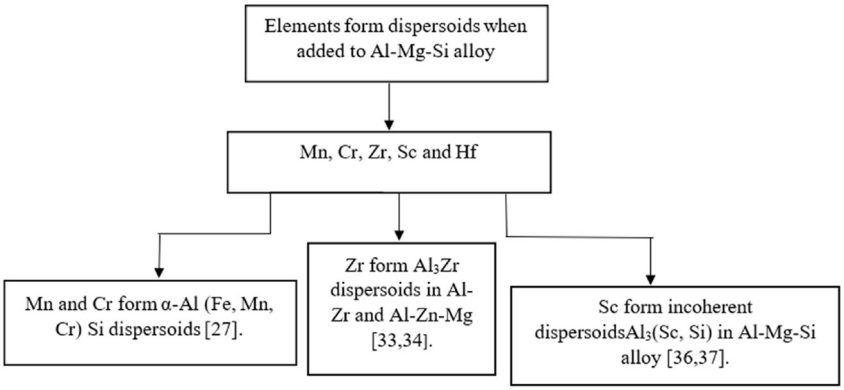

Fig. 4 – Describe element's Dispersoids phases with 6xxx AA.

critical and affects the alloys' mechanical properties. To get alloys to behave at their best, a Mg/Si solubility ratio close to 1.74 is required [15].

The nucleation of β″ during paint baking is negatively impacted by NA at room temperature (RT), which weakens these alloys. These alloys become weaker and develop the finest micro-structure under peak hardness conditions, along with the GP zones, when even a small amount of the β″ phase precipitation occurs [23,24,25].

One of the best methods for reducing the negative effects of NA in 6xxx AA is micro-alloying. In the first process, the atoms of the solute, such as the elements Cu and Ag, alter the atomic structure of the precipitates [26–28]. Although Ag is superior to Cu in terms of improving precipitation kinetics, it is not the best element for reducing the harmful effects of NA [24,25,29,30]. This review paper provides a comprehensive study of various elements which has been added to 6xxx AA to reduce the harmful effect of NA and improve mechanical properties.

1.1. *Influence of solute element in 6xxx aluminium alloys*

The development of primary phases and dispersoids, the agglomeration of grains, precipitation, and other processes can all be impacted by all of these characteristics. Fig. 3

Table 1 – Identified precipitate phases in 6xxx AA. Data were taken from Ref. [17].

Phases	Chemical Formula	Space group	Lattice parameter
GP Zones	Variable	C2/m	a = 1.480, b = 0.4050, c = 0.6480, β = 105.30°
β″	$Mg_{6-x}Al_{1+x}Si_4(0 \leq x \geq 2)$	C2/m	a = 1.5160, b = 0.4050, c = 0.6740, β = 105.30°
β′	$Mg_{1.8}Si$	$P6_3/m$	a = b = 0.7150, c = 0.6740, γ = 120.0°
U1	$MgAl_2Si_2$	$P\bar{3}m1$	a = b = 0.4050, c = 0.6740, γ = 120.0°
U2	MgAlSi	Pnma	a = 0.6750, b = 0.4050, c = 0.7940
B′	$Mg_9Al_3Si_7$	Hexagonal	a = b = 1.040, c = 0.4050, γ = 120.0°
B	Mg_2Si	$Fm\bar{3}m$	a = 0.6350

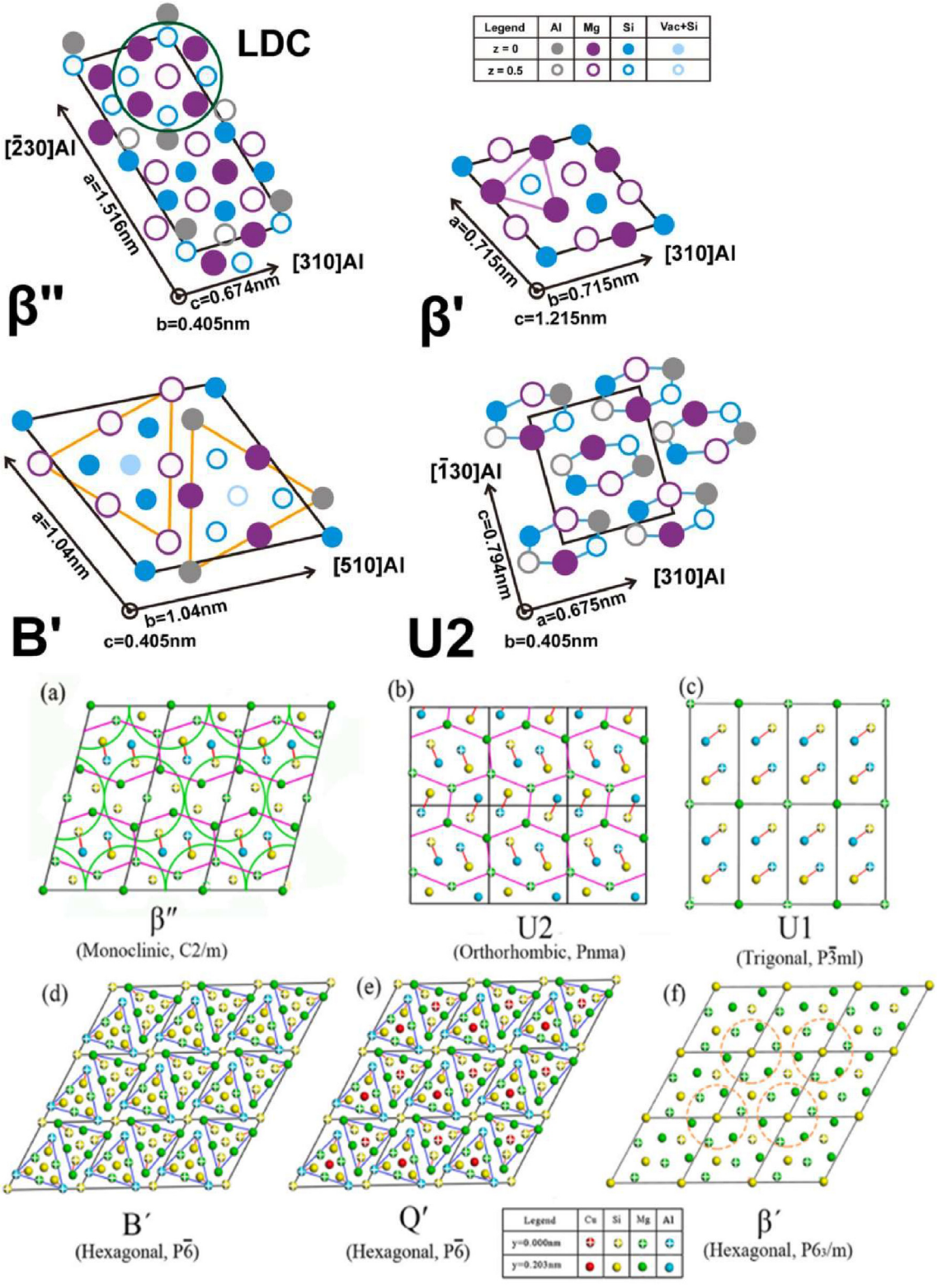

Fig. 5 – Unit cells for β″, β′, B′, Q′, U1 and U2 are shown schematically. Adapted with permission from Refs. [53,54].

displays a list of the classified functions for every element that affects aluminium alloy characteristics. The impact of dispersoids is discussed in the next section, summarising the roles played by the various segments [31] (see Fig. 4).

1.1.1. *Elements form dispersoid*

The primary phase is created when Mg and Si combine to form Mg_2Si during the solidification of 6xxx AA [31]. The primary focus of this review paper is on the formation of hardening

metastable precipitates that happen during high-temperature alloy processing procedures when Si and Mg alloy concentrations are less than the solubility of Mg_2Si.

In general, the precipitates in 6xxx AA are not directly impacted by the transition elements that give rise to primary phases and dispersoids. However, dispersoid production somewhat affects precipitation.

For instance, the potential strength increase is decreased when coarse Mg_2Si particles preferentially nucleate on dispersoids following solutions or extrusion. The term for this occurrence is quenched sensitivity [32,33,34]. Denser, higher-strength alloys, such as AA6082, are more likely to experience this phenomenon [35,34].

1.1.2. *Grain refinement elements*

Grain refinement is typically necessary to reduce casting and solidification flaws. B and Ti are common elements in this usage. It is well known that a peritectic process creates the Al3Ti interface layer on TiB_2 particles, which act as the nucleation sites for grains in aluminium alloys [36]. Some transition elements act as sites for grain nucleation in solidifying aluminium alloys because of their peritectic reactivity [37]. Extrusion and rolling are two examples of heat deformation procedures that have an impact on the final grain sizes and structures. The atomic structures of the precipitates are not directly affected by these grain-refining elements, but grain size is a crucial aspect in the precipitation of metastable precipitates [38,39].

1.2. *In 6xxx alloys, precipitate phases*

Si and Mg contents frequently fall below the solubility's upper bound in wrought 6xxx AA (an Al–Mg_2Si pseudo-binary phase diagram can be found elsewhere) [40]. Nucleation,

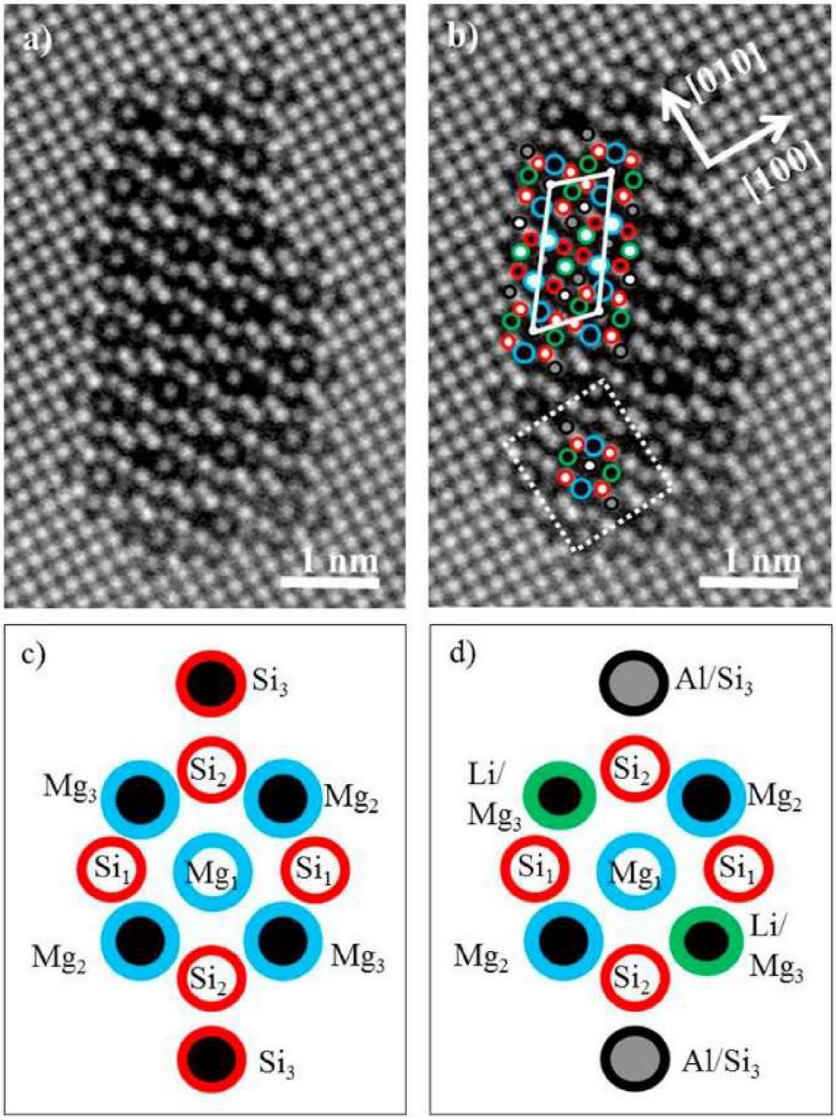

Fig. 6 – (a) Picture of a β″ precipitate cross-section in RXL0 that has been "Smart Aligned". (b) Single β″-the eye marked inside the white dashed square and a white, solid line parallelogram formed a unit cell of β″. (c) The β″eye as it has been characterised in earlier investigations. (d) The eyes of the same heights in β″ are directly equivalent to the β" having Li at Mg3 place. With permission from the cited source [55].

transformation, and growth are three phase transitions that the alloy experiences during AA; all three are thermally stable and soluble phases at the designated ageing temperature [41]. Negative free energy changes control nucleation, whereas volume-free energy and interfacial control the rate of change and growth. The precipitation of the 6xxx AA occurred in the sequence shown below.

SSS ⟶ Atomic Clusters [42–44] ⟶ GP zone ⟶ β″ [45,46] ⟶ β′ [47,48], U1 [49], U2 [43] ⟶ β [50,51], Si [52].

According to Table 1 and Fig. 5, each ordered metastable precipitate phase found in 6xxx AA has a structural unit cell model [17,53,54].

The bulk of age-hardenable 6xxx alloys is strong due to primary hardening phase, which is the coherent β" phase. In addition to an alloy's composition and thermo-mechanical processing, local features such as dislocation, grain boundary created by rolling or stretching, dispersoids, etc, also have a role in the phases that are created for a given alloy.

The organization's composition and structure of β″ have been hot topics for debate during the last 20 years. First, the composition and crystal structure of Mg_5Si_6 were determined [45,49]. Al was suggested to be incorporated into β″-$Mg_5Al_2Si_4$ through additional characterisation method development [43]. There have been several atom probe tomography (APT) experiments that have gained popularity recently, have and gained acceptance recently [50–52]. There may be compositional changes in the Mg–Al atoms, depending on several density functional theory (DFT) investigations, $Mg_{(6-x)}Al_{(1+x)}Si_4$ ($0 \leq x \leq 2$) [56]. There are specifics regarding this conversation and disagreement available [57]. Cu [58] and Zn [59] do

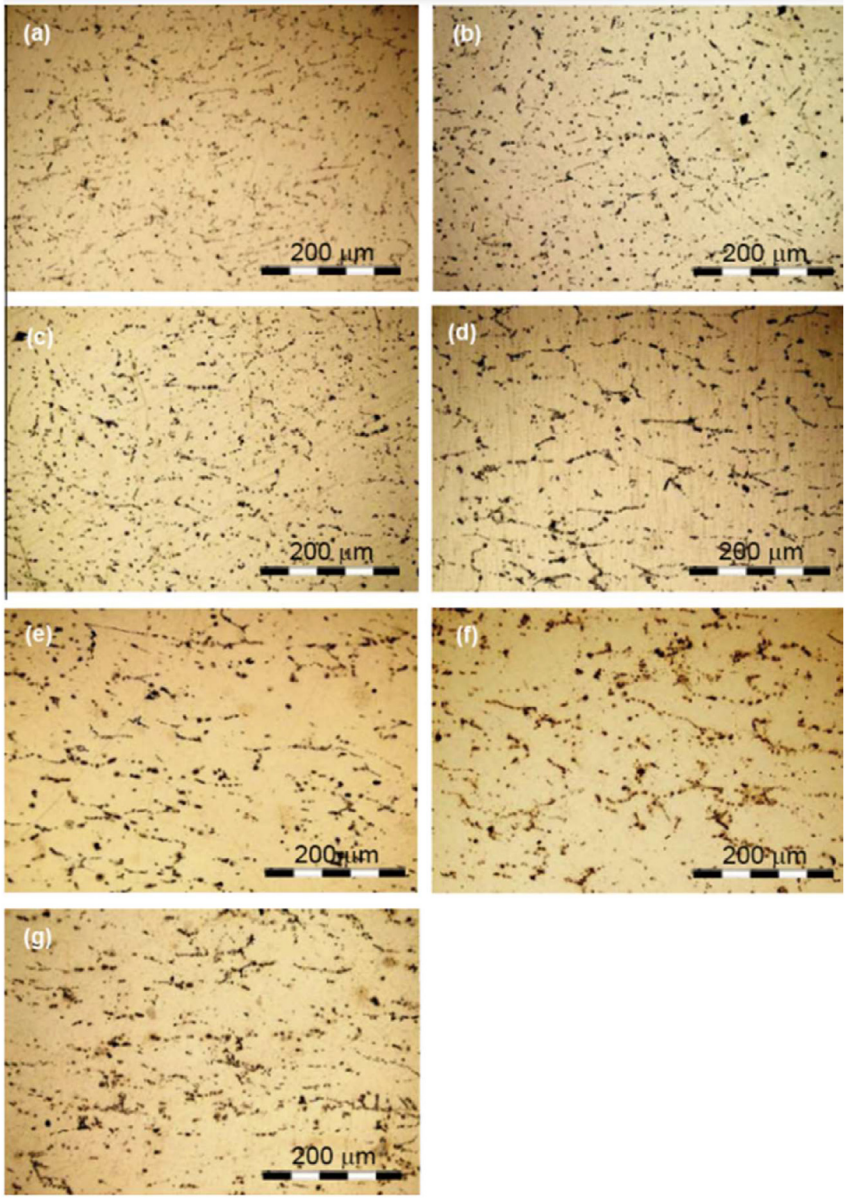

Fig. 7 – Images of samples taken under an optical microscope at temperatures ranging from (a) T6 and (b) to (g) T8. From least to greatest, the following cold reduction samples were aged at 175 C for 10 h: (a) 0%, (b) 10%, (c) 20%, (d) 30%, (e) 40%, (f) 50%, and (g) 60%. Adapted with permission from Ref. [62].

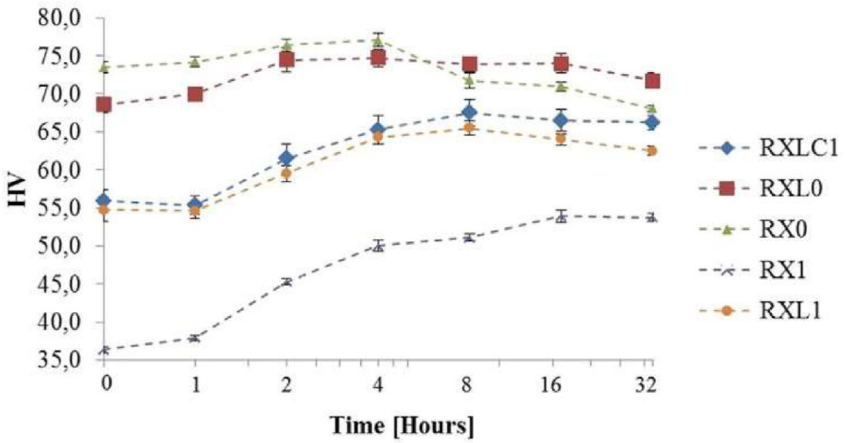

Fig. 8 – Vickers hardness plotted against artificial ageing time at 195 °C. The reference alloys RX0 (top) and RX1 (bottom) are described as being lean and dense, respectively. The letters "L" and "C" in an alloy stand for lithium and/or copper, respectively. Data taken from Ref. [55] (See Table 2).

Table 2 – Alloy composition in RX0 (AA6060 reference alloy). Data taken from Ref. [55].

Alloy	Si	Mg	Cu	Li	Fe	Mn	HV
RX0 wt.%	0.45	0.37	–	–	0.20	0.03	77
RX1 wt.%	0.37	0.32	–	–	0.20	0.03	50
RXL0 wt.%	0.440	0.290	–	0.026	0.20	0.030	75
RXLC1 wt.%	0.370	0.320	0.050	0.006	0.200	0.030	65
RXL1 wt.%	0.420	0.270	–	0.013	0.200	0.030	65

Table 3 – Alloy with different weight percent. Data taken from Ref. [62].

Alloy composition	Li (wt.%)	Mg (wt.%)	Si (wt.%)	Al (wt.%)
Balanced	3	0.50	0.20	Bal.

not appreciably affect the compositions. Additionally, it has been discovered that Li or Ge-containing alloys possess numerous stacking configurations of the eye-like β″ molecules, known as β″eyes (see Fig. 6) [22,55,60].

2. Material analysis and systematic review

In this section the change in the microstructural and mechanical properties of alloys while the addition of Li, Cu, Zn and Ag in 6xxx AA.

2.1. *Participating elements in metastable precipitation*

2.1.1. *Lithium (Li)*

2.1.1.1. *Microstructural analysis.* The addition of lithium (Li) to aluminum alloys, specifically the 6xxx series AA, results in

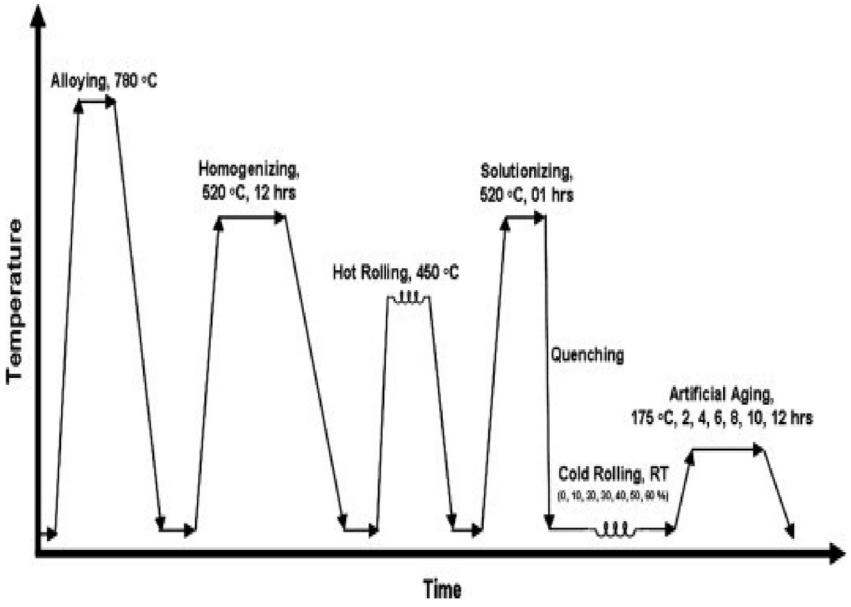

Fig. 9 – A schematic diagram outlines the thermomechanical treatment process. Data taken from Ref. [62].

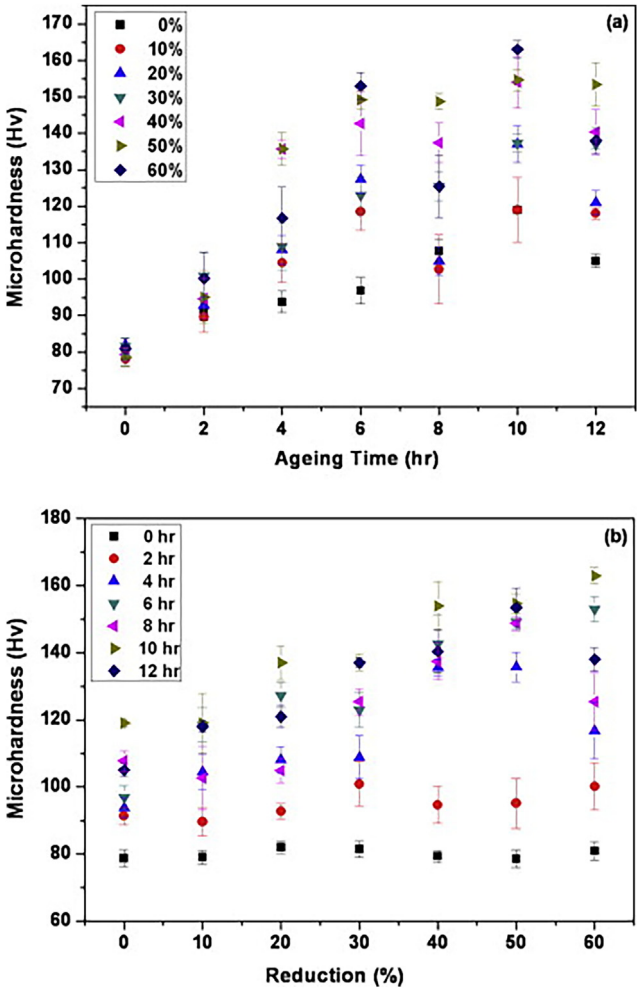

Fig. 10 – (a) For various levels of cold work, hardness vs. ageing time and (b) For various ageing times, hardness versus cold work. Data taken from Ref. [62].

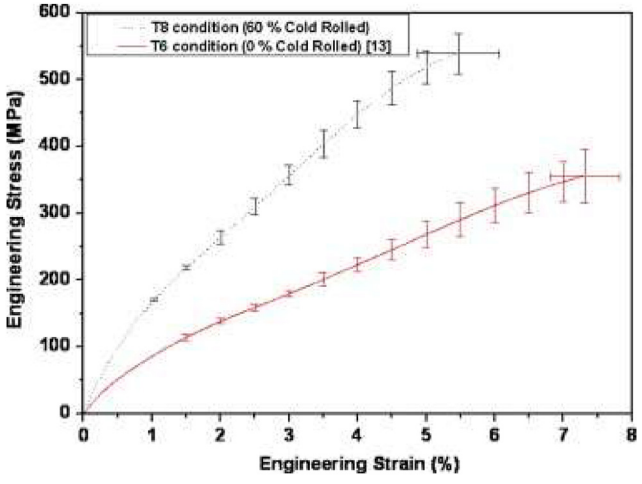

Fig. 11 – Plots of engineering stress-strain comparing the mechanical characteristics of the alloy treated at T6 condition (0% cold rolling) and T8 condition (with 60% cold rolling). Data taken from Ref. [62].

reduced alloy density due to Li's properties. Li can enhance age-hardening behavior in these alloys, infiltrating the hardening phases without changing the precipitation sequence significantly. This alloy's microstructure, observed through transmission electron microscopy (TEM), reveals Li's influence on hardening phases [55,61]. Li occupies Mg3 sites in β″, as it is energetically favourable to do so. Density functional theory studies support this, showing Li's preference for Mg3 sites in β″, leading to a notable replacement of Mg by Li [55].

Fig. 7(b)–(g) display the optical micrographs of 10%, 20%, 30%, 40%, 50%, and 60% cold-rolled samples, respectively, under the T8 condition, processing route shown in the figure and the alloy chemical composition shown in the table [62]. Fig. 7(a) shows the microstructures of a 0 % cold-rolled sample under T6 conditions. On the micrographs, only two phases can be distinguished: a matrix phase and grain boundary phase with a less size variation. As the percentage of cold reduction increases, it was observed that particles in the second phase grew longer and more perpendicular to the direction of rolling [62].

2.1.1.2. *Mechanical properties*. In Fig. 8, the hardness curves of RX0 and RX1 are compared, based on data from previous studies. RX1 performs the poorest, with its curve being significantly lower than other alloys. RXL0, a variation of RX0, substitutes Li atoms for a quarter of its Mg atoms, resulting in the same solute atomic concentration. However, the solute weight is 9.1% less as referenced in Table 2 [55]. Due to the addition of lithium, RXL0's peak hardness exceeds that of RX0 for extended ageing durations, compensating for the reduced strength in leaner references [55].

The alloy from Table 3 was prepared through various treatments including casting, homogenization, hot and cold rolling, and ageing, as illustrated in Fig. 9 [62] (see Figs. 10–12).

The hardness results revealed that the age-hardening effect was more pronounced under the T8 condition as cold work increased, particularly past 30% reductions. The highest hardness for the T6 condition was 119HV after ageing [62] (Fig. 10). The alloy's mechanical properties, such as yield and tensile strength, also improved notably under the T8 condition after artificial ageing [62].

However, as Li content ranged from 2 to 3 wt.%, there was an increase in ageing effects at the expense of ductility. In a different process, the alloy's composition was altered by varying Li percentages, as shown in Table 4 [61].

Post-processing, the hardness of the extruded alloys directly correlated with their Li content (Fig. 13(a)) [61]. The stress-strain curves of different alloys, depicted in Fig. 13(b), showed that while alloy-1 was similar to the 6063 alloys in the T6 condition, alloy-2 had reduced strengths and alloys 3 and 4 exhibited significant increases in these properties [61].

2.1.2. *Copper (Cu)*

2.1.2.1. *Microstructural analysis*. In alloys that fall under the 2xxx class, Cu acts as the primary alloying element. Cu is a component in 6xxx AA that increases peak hardness. The precipitate sequence of the Al–Mg–Si system is changed by the addition of Cu (0.4 wt.%) as shown below:

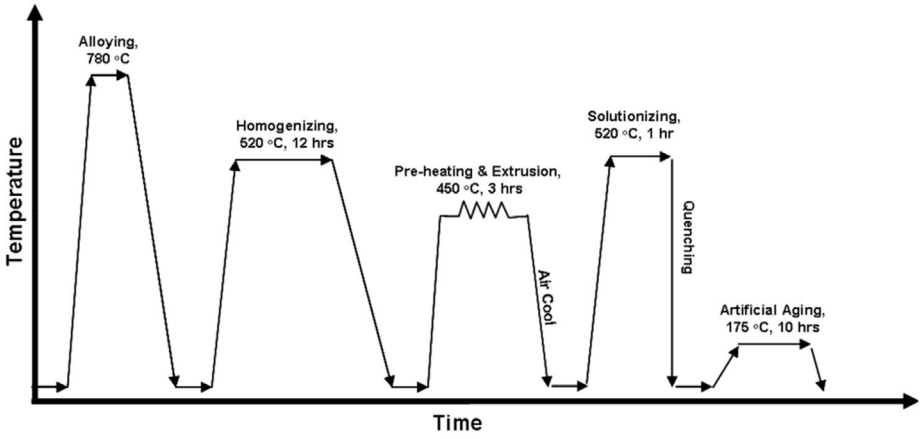

Fig. 12 – A schematic diagram outlines the thermomechanical treatment process. Data taken from Ref. [61].

Table 4 – Alloy with different weight per cent. Data taken from Ref. [61].

Sample	Li	Mg	Si	Zr	Al
Alloy-1	0	0.82	0.42	0.12	Bal.
Alloy-2	1.20	0.85	0.44	0.11	Bal.
Alloy-3	2.20	0.84	0.42	0.11	Bal.
Alloy-4	3.20	0.84	0.43	0.13	Bal.

SSS ⟶ Atomic clusters [23,63] ⟶ GP Zones [6] ⟶ β″ [43,49], L [64], C [65], QP [66], QC [65,66] ⟶ β′ [48], Q′ [67,68],Q [69].

In addition to producing a variety of precipitates, including L, C, QP, and QC at the height of ageing and Q′ in the over-aging stage, this solute redistribution also stops the growth of β″. These precipitates can still be seen at particular chemical compositions and ageing conditions, despite being less coherent than β″. The L phase exhibits compositional variations and has a chaotic structure with a lath morphology [64]. Additionally, it was shown that the Mg/Si ratio is crucial for the creation of the L phase monoclinic unit cell and a plate-shaped morphology characterises the C phase [70–72]. The L and C phases, which are thought to be the antecedents of the Q′ phase, are both extended [66]. The reported QC periodicity of 0.7 nm may be the β'_{Cu} phase, and the measured QP periodicity of 0.4 nm may be a disordered phase linked to the Si network. The Q′ phase, which is found in ageing-related conditions and has Cu replaced with Al, is isostructural to the B′ phase [70]. Different orientation interactions between Q′ precipitates and the aluminium matrix were found to exist. In equilibrium with the Q phase are $Al_3Cu_2Mg_9Si_7$ composition has been suggested. Many reports demonstrate slightly varying Q components, $Al_4Cu_2Mg_8Si_7$, within $Al_xCu_2Mg_{12-x}Si_7$ [73]. Fig. 14 and Table 5 shows the cell models for the metastable precipitate phases in the Cu-containing 6xxx AA (see Table 6).

Cu increases the numerical density of precipitates when added in modest amounts (0.1 wt.%), as was seen in 6060 alloys [76,77]. The structurally perfect β″ and disordered sections can coexist, as shown in an example in Fig. 15. In the disorganised region, Cu atomic columns were discovered. The fragments, which cover the whole length of a precipitate and are needle-shaped, are frequently seen in disordered

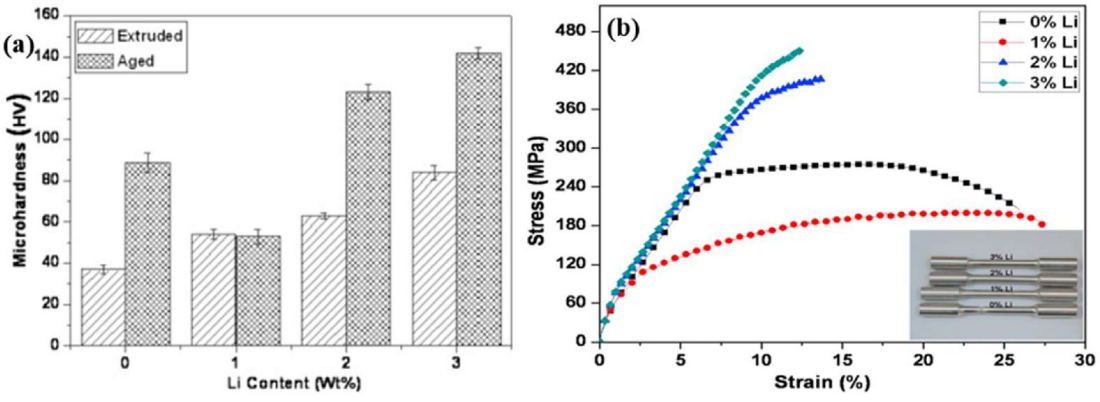

Fig. 13 – (a) Extruded and aged alloys with varying Li content's hardness profiles, (b) Stress-strain plots for the four alloys in their aged state from engineering. Data taken from Ref. [61].

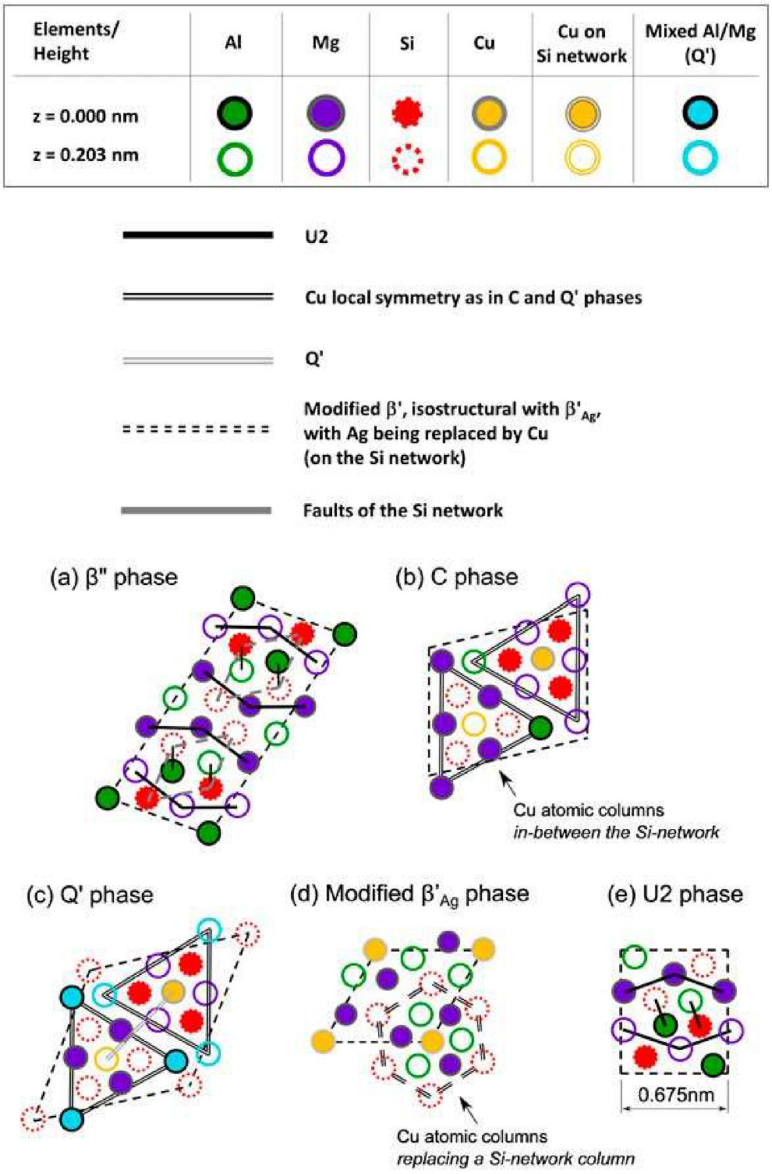

Fig. 14 – Al–Mg–Si alloys with metastable precipitate phases containing Cu or Ag are represented by structural unit cell models. In the Q′ phase, Cu atomic columns are situated between the Si network columns, whereas in the Ag/Cu phase, they are situated on the Si network. With permission from the cited source [74].

precipitates and have also been found in Li, Zn, and/or Ge alloys that contain Al-Mg-Si [78]. In a recent investigation, these findings were also made in disordered precipitates containing copper [79]. The same principle applies to Si-network layouts for columns even for unstable structures with copper [80].

The various observations could be the result of various heat treatments and varying observed precipitate sizes. The

Table 5 – Precipitate phases found in 6xxx AA containing copper. Data taken from Ref. [75].

Phases	Compositions	Space groups	Lattice parameters
L	Variable	Disordered	
C	$Mg_4AlSi_{3.3}Cu_{0.7}$	$P2_1/m$	$a = 1.0320$, $b = 0.4050$, $c = 0.8100$, $\beta = 100.90°$
QP	Unknown	Hexagonal	Probably a disordered phase with the Si network
QC	Unknown	Hexagonal	Probably the β'_{Cu} phase
Q′	$Al_3Cu_2Mg_9Si_7$		$a = b = 1.0320$, $c = 0.4050$, $\beta = 120°$
Q	$Al_3Cu_2Mg_9Si_7$		$a = b = 1.0320$, $c = 0.4050$, $\beta = 120°$

Table 6 – Chemical composition of the alloys A and B which has been examined in this work. Adapted with permission from Ref. [54].

Alloy	Si	Mg	Cu	Mn	Fe
A	1.08	0.063	–	0.06	0.13
B	1.11	0.62	0.06	0.06	0.16

Si3/Al site appears more advantageous for Cu inclusion in β″ in any case, and DFT calculations support this [81] shown in Fig. 16. It has been reported that precipitates with a modest β″cross section contained Cu atomic columns at Mg1 sites [82].

From a TEM image perspective, Fig. 17 summarises the Nano-precipitates produced in the two alloys at the early (1 h), intermediate (2 h), late (2 d), and well-over-aged (3 weeks) ages. Both alloys exhibit significant numbers of needle-like precipitate particles at the under-aged and peak-aged stages, but the majority of precipitates undergo morphological changes to lath- or rod-like morphology and increase in size during the over-aged stage. When comparing the precipitate distribution of alloys B and A, alloy B exhibits a finer precipitate distribution.

ALLOY A: SSS ⟶ Atomic Clusters [42–44] ⟶ GP zone ⟶ β″ [45,46] ⟶ β′ [47,48], U1 [49] ⟶, U2 [43] β [50,51], Si [52].

ALLOY B: SSS ⟶ Atomic clusters [23,63] ⟶ GP Zones [6] ⟶ β″ [43,49], L [64] ⟶, C [65], QP [66], QC [65,66] ⟶ β′ [48], Q′ [67,68],Q [69].

Fig. 18 (a) depicts the GP zone in the alloy B's under-aged state, while (b) and (c) display two β″ precipitates in the alloy B's peak-aged state. The LDC (Low-density cylinder) is visible within a framework of dashed green circles within the GP zone, whose layout is reminiscent to that of the β″ phase [83]. Fig. 18(b) and (c) have the same monoclinic structure which are marked by red line and the two β″ precipitates are present. Just the two columns between the LDCs, which are denoted by dashed yellow circles, change significantly in intensity. These columns have been termed satellite columns by Mørtsell et al. [83]. In general, Fig. 18(b) columns have lower intensities than those in Fig. 18(a) and (c) [83].

Fig. 19, Part (a) and (b) of the figure give the HAADF images of alloy A and B. In the direction of Al, there are so many needle-like precipitates which are reported to be β″ phase. In this image, one more thing is observed i.e., the precipitate of alloy B is more uniform than that of alloy A. Scanning TEM(STEM) of alloy A is shown in Fig. 19 (c) and (d) [84].

Whereas Fig. 20(a) In AA6005 addition of 0.5 wt.% Cu has been done which forms needle shaped phases formed with β″ precipitate form after doing artificial ageing at 175 °C for 8 h. After

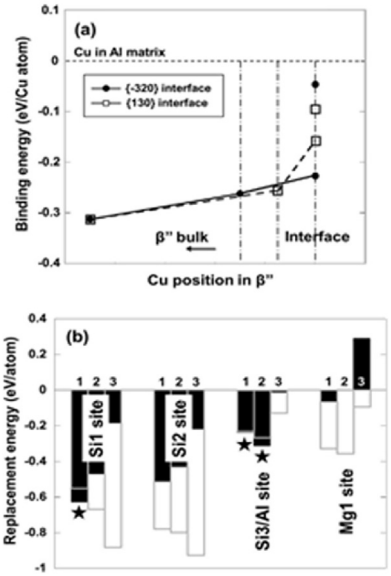

Fig. 16 – (a) Cu-β′′ interaction research using computational (DFT). (a) Cu binding energies for specific Si3/Al site locations in β′′ -$Mg_5Al_2Si_4$ interface, right vertical line. Other vertical lines: migration into β′′ bulk along {—320} and {130} interfaces, respectively, (b) shows three possible β′′ configurations for Cu (black bars) and the alternate solute atoms Mg/Si (white bars) on selected sites, namely $Mg_4Al_3Si_4$, $Mg_5Al_2Si_4$, and Mg_6AlSi_4. At the omitted locations Mg2, Mg3, Cu scarcely binds. The dark stars at the matching β′′ configurations exhibit favourable Cu integration sites. Adapted with permission from Ref. [81].

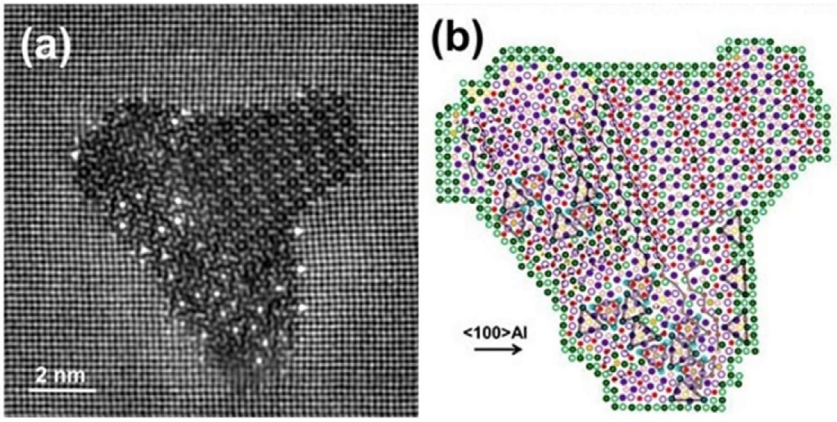

Fig. 15 – A proposed atomic overlay of the precipitate component can be seen in the dashed white square in (a) along with a HAADF-STEM image of an alloy cross-section made up of a disordered precipitate that contains Al-0.47 wt%Mg-0.42 wt%Si-0.10 wt%Cu. (b) The unit cell of β′′ is indicated through a white solid line. With permission from the cited source [74].

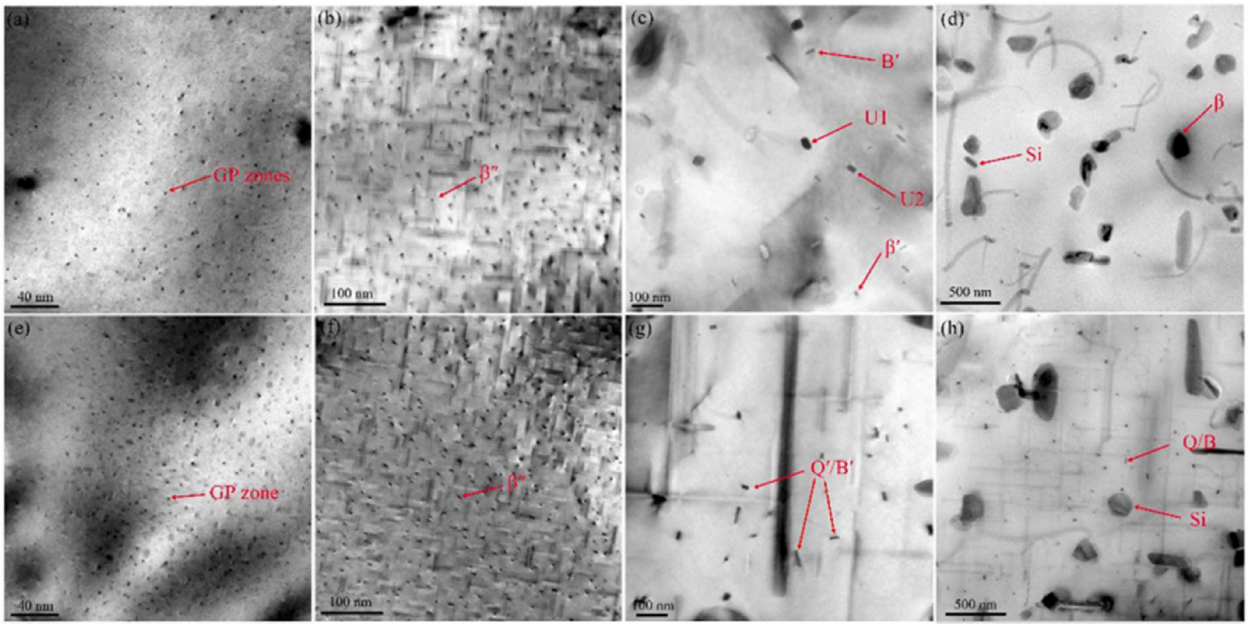

Fig. 17 – Overview of the precipitates seen in alloys (a–d) A and (e–h) B under (a, e), peak (b, f), over (c, g), and well (d, h) aged conditions is shown in the TEM image. With permission from the cited source [54].

ageing the precipitates are seen shown below in Fig. 20(b). The over-ageing phase of Cu containing will form the Q′ [85].

In both the un-deformed and the pre-deformed situations, the highest hardness was produced by Cu additions, which led to finer microstructures. The predeformed and undeformed conditions can be understood with the help of Fig. 21(a) and (b) [76].

In the undeformed condition, homogeneous patterns of precipitates were seen for both alloys (Fig. 22 (a) and (b). Contrarily, in the predeformed state, heterogeneous

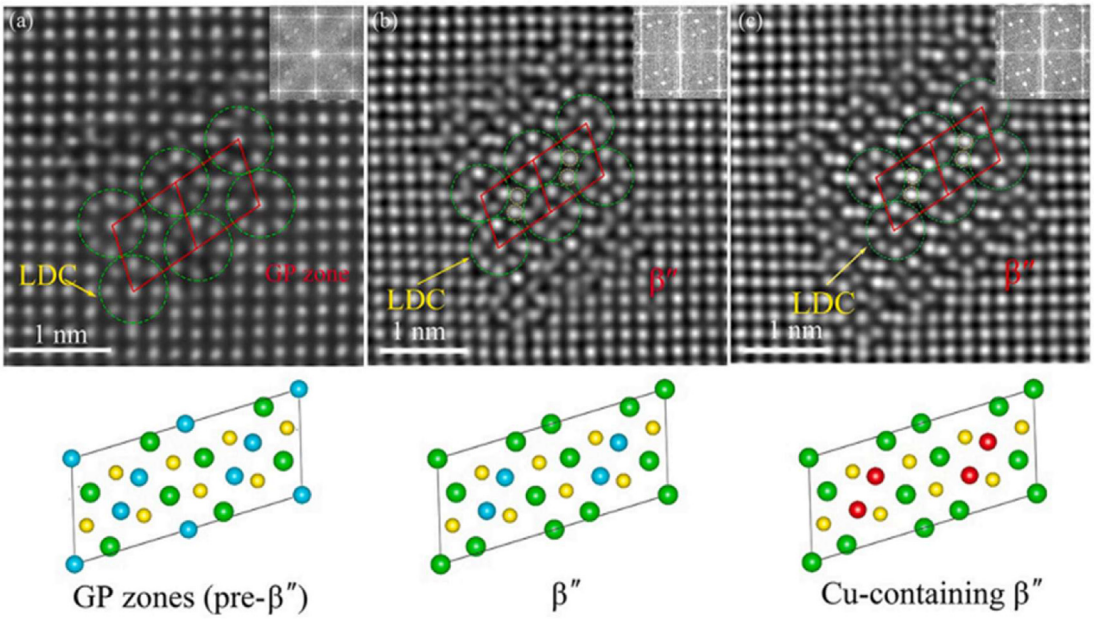

Fig. 18 – HAADF-STEM pictures of (a) the GP zone and (b) β″ precipitates generated in alloy B without Cu incorporation and (c) with Cu incorporation at the peak aged state. Green dashed circles outline LDCs, yellow dashed circles outline satellite columns, and red lines outline cells. After each picture, you'll see a structural model of one of the three precipitates. With permission from the cited source [54].

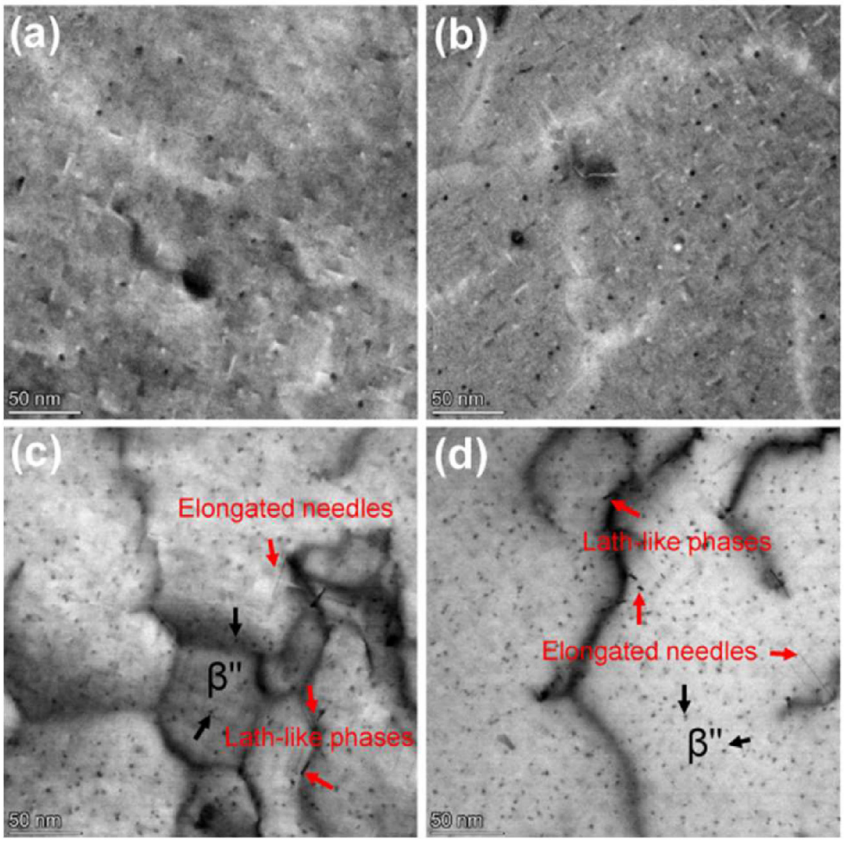

Fig. 19 – After paint baking, HAADF images of (a) alloy A and (b) alloy B under 3% pre-strain; (c) and (d) STEM images of alloy A and alloy B under 3% pre-strain. Taken along the Al zone axis. With permission from the cited source [84].

distributions linked to dislocation lines were observed (Fig. 22(c) and (d) [76]. The microstructures generated by pre-deformation were coarser in comparison to undeformed conditions. When measured values for conditions (a), (c) and (b), (d) are compared, it is evident that the alloy with the higher amount of Cu (d) had less of a coarsening effect. The examined

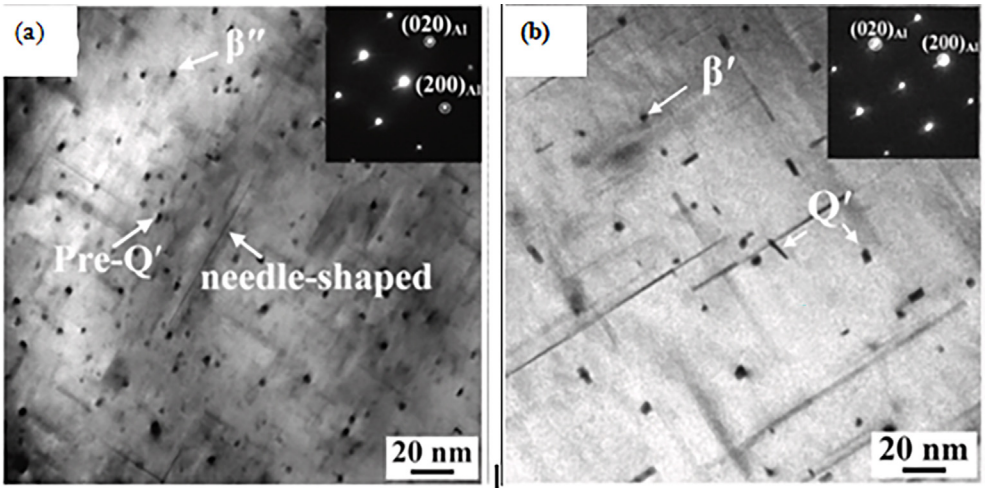

Fig. 20 – TEM and HRTEM pictures of the precipitates in test alloys after an artificial 8-h ageing period at 175 °C: (a) 0.5 wt.% Cu, for 1000 h at 150 °C: (b) 0.5 wt.% Cu. With permission from the cited source [85].

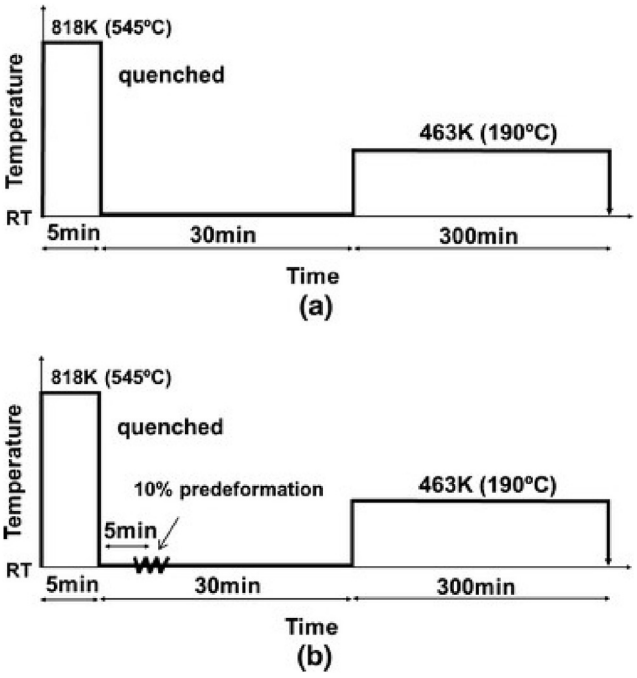

Fig. 21 – Thermomechanical histories for the situations that are (a) undeformed and (b) 10% predeformed. Adapted with permission from Ref. [76].

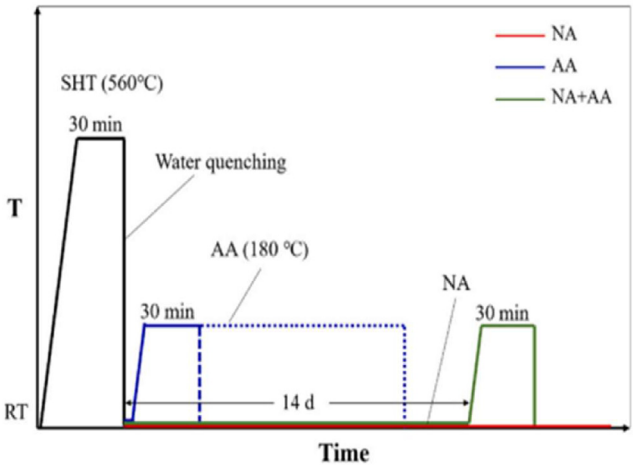

Fig. 23 – Schematic diagram of the heat treatment profile for all alloys. Data taken from Ref. [86].

alloy that was subjected to 0.10 wt percent Cu and 10% predeformation (condition (d)) had the maximum volume fraction of precipitates [76].

The effect is to increase the hardness contributions of various parameters to see how Cu additions alter the predeformation's effect on hardness. There are four potential separate origins: Contribution from the solid solution, the

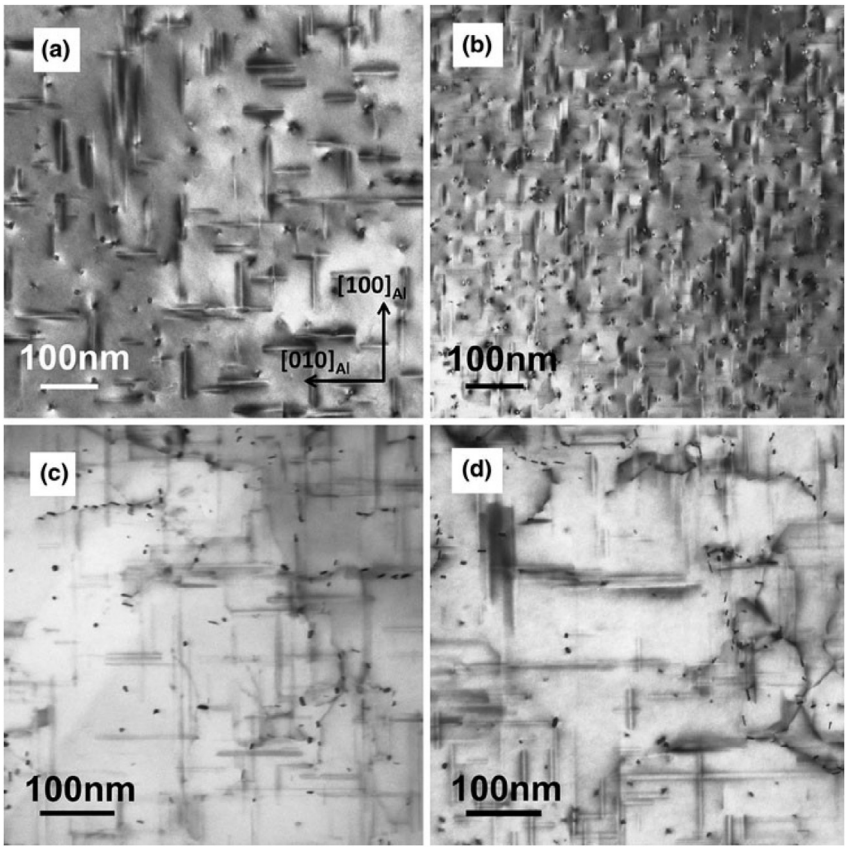

Fig. 22 – Bright-field TEM along the 001 Al directions of alloys containing 0.01 wt percent Cu, 0.10 wt percent Cu, and 0.01 wt percent Cu and 0.10 wt percent Cu under undamaged conditions Copper is produced with a 10% predeformed state after 300 min of isothermal heat treatment at 463 K (190 °C). With permission from the cited source [76].

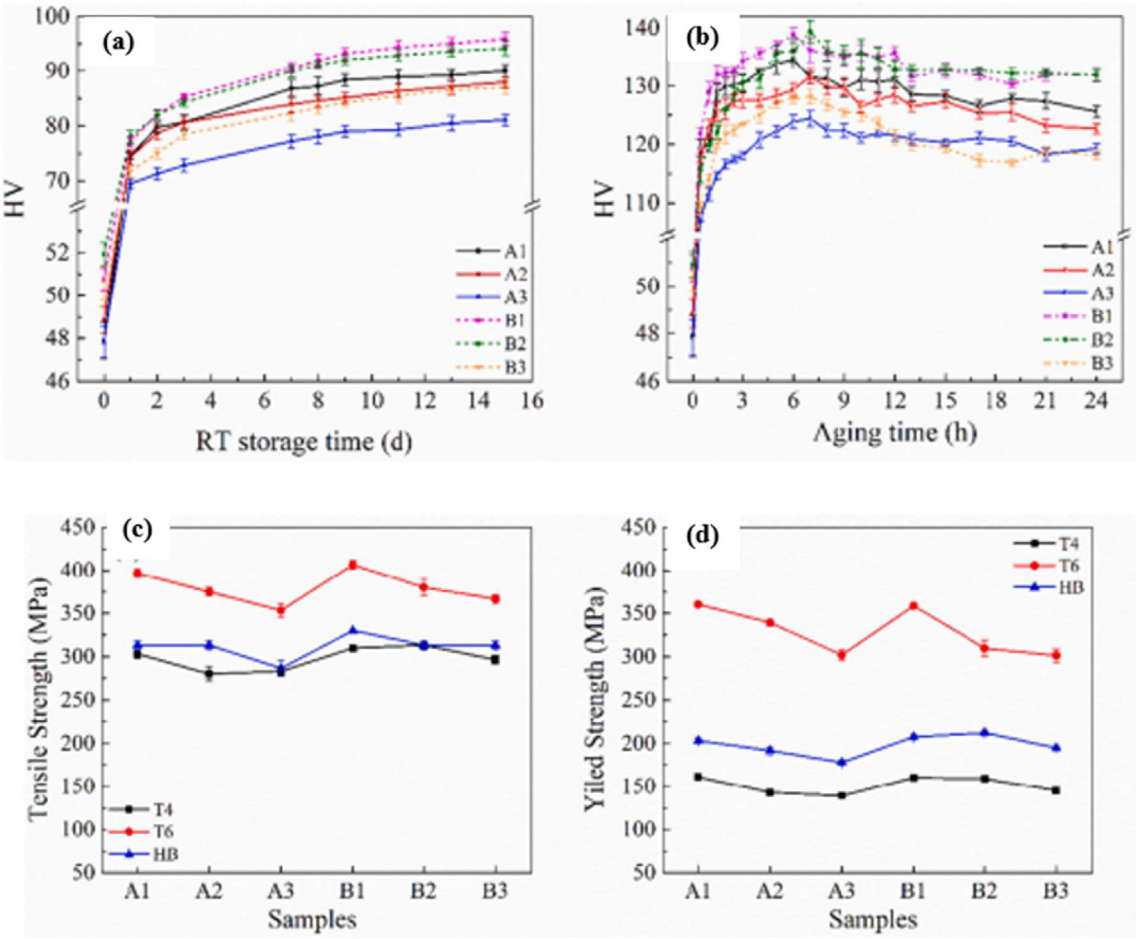

Fig. 24 – (a) Vickers hardness of the 6 alloys in natural ageing (b) Vickers hardness of the alloys in artificial ageing after water quenching, (c) Tensile properties of the 6 alloys in ultimate tensile strength (d) Tensile properties of the 6 alloys in yield strength. Data taken from Ref. [86].

Table 7 – Alloys with different chemical composition. Data were taken from Ref. [86].

Alloy	Si	Cu	Mg	Mn	Fe
A1	0.68	0.7	1.02	0.06	0.15
A2	0.53	0.7	1.16	0.06	0.15
A3	0.42	0.7	1.26	0.06	0.15
B1	0.68	1.0	1.02	0.06	0.15
B2	0.53	1.0	1.16	0.06	0.15
B3	0.42	1.0	1.26	0.06	0.15

dislocations, the precipitates, and the pure Al matrix (HV_{pure}, HV_{ss}, HV_{dis} and HV_{pre}). So, a straightforward summation can be used to express the overall difficulty [76].

$$HV = HV_{pure} + HV_{ss} + HV_{dis} + HV_{pre}$$

2.1.2.2. *Mechanical properties*. The study investigates the precipitation characteristics in Mg-rich, high-Cu alloys to advance Al–Mg–Si based alloy development. Six alloys underwent various processes like casting, homogenizing, and ageing, with solution treatment at 560 °C, as shown in Fig. 23 [86].

Fig. 24(a) and (b) depict hardness trends during natural and artificial ageing, respectively. Natural ageing reveals a swift initial hardness surge, then a steady climb. Group B alloys consistently outperformed group A in hardness. Variations in hardness based on Mg/Si ratios and copper content are highlighted in Fig. 24(c) and (d) [86]. While increased Mg/Si ratios mildly dampened bake hardening, augmenting copper content enhanced it [86] (see Table 7).

Table 8 – Al–Mg–Si(-Cu) alloy compositions under study. Data taken from Ref. [87].

Alloy	Al	Si	Mg	Cu	Fe	Mn	Cr
S at./wt.%	Bal.	0.85/0.88	0.80/0.72	0.01/0.03	0.12/0.24	0.25/0.51	0.08/0.16
C at./wt.%	Bal.	0.85/0.88	0.71/0.64	0.04/0.09	0.10/0.20	0.22/0.45	0.07/0.14
M at./wt.%	Bal.	0.62/0.64	0.86/0.77	0.1/0.23	0.13/0.26	0.13/0.26	0.01/0.02

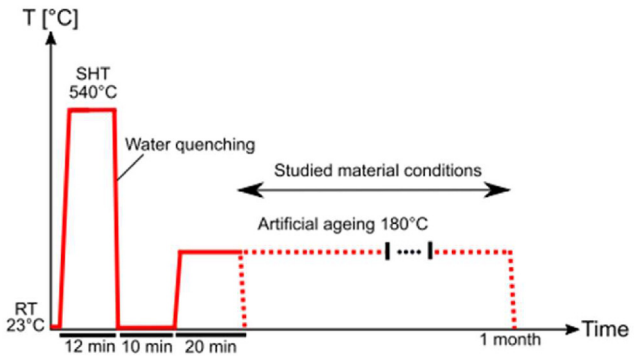

Fig. 25 – Schematic diagram of the heat treatment profile for Al–Mg–Si(-Cu) alloys. Data taken from Ref. [87].

Another alloy, detailed in Table 8, experienced a unique heat treatment. After solution heat treatment, these samples underwent artificial ageing at 180 °C with different durations, as detailed in Fig. 25 [87].

Fig. 26(a) shows varying peak hardness durations during ageing, with Alloy M outshining Alloys S and C. Regarding σy values, Alloy C surpassed others under specific conditions, as shown in Fig. 26(b) [87].

2.1.3. *Zinc (Zn)*

2.1.3.1. *Microstructural analysis*. 2In Al–Zn–Mg (-Cu) alloys, which are characterised as 7xxx series aluminium alloys, Zn serves as the primary alloying element and produces a variety of metastable plate-shaped precipitates known as β" phases. Numerous investigations looked into how Zn affected precipitates in Al–Mg–Si alloys [88,89]. The pre-β″, β″, disordered, and L phases of the observed precipitates along <001>Al show that Si predominates over Zn as the nucleation agent [88]. There is no record demonstrating the production of novel precipitate forms for Zn additions to 6xxx AA (up to 1 wt.%) [89]. Precipitates become disorganised when Zn is added. In this way, the Zn distribution is comparable to the Cu distribution in similarly disordered precipitates shown in Fig. 27 [88].

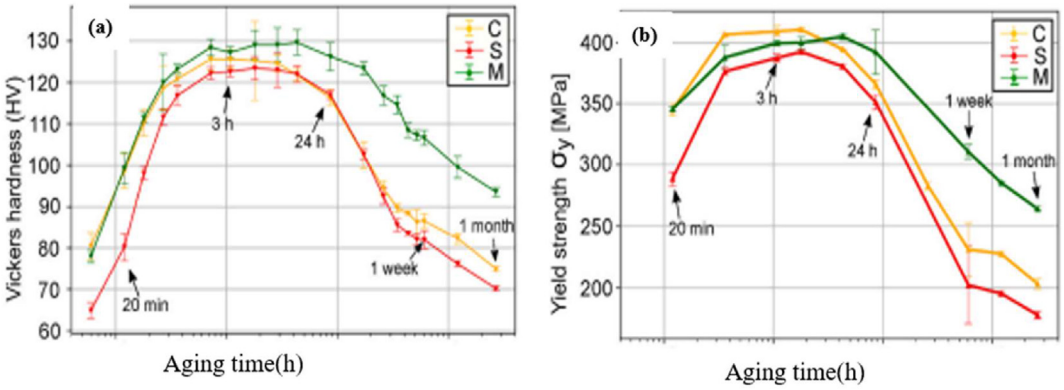

Fig. 26 – (a) Vickers hardness (HV) and Material tensile properties obtained from true stress-strain curves, showing (b) yield strength. Data taken from Ref. [87].

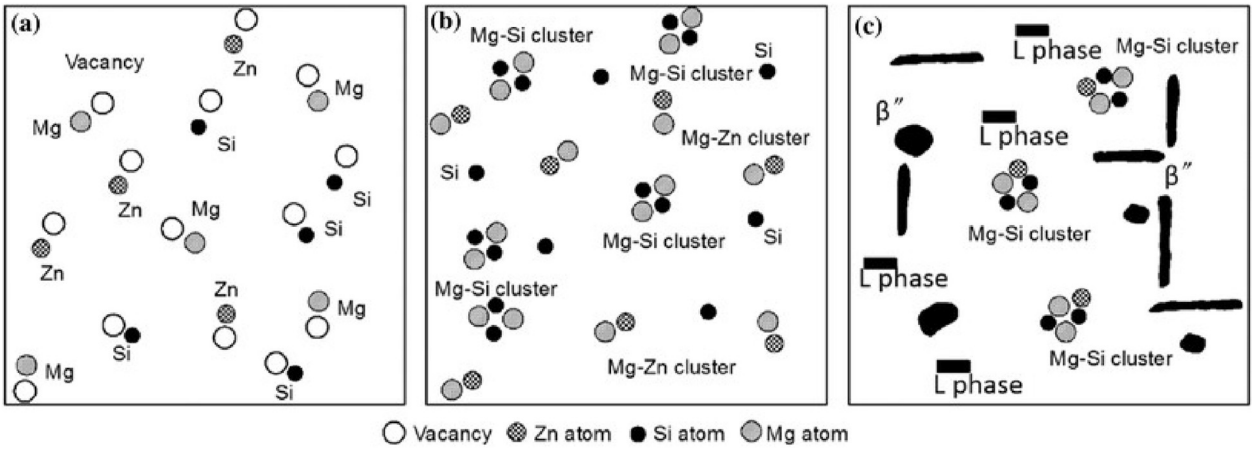

Fig. 27 – Al–Mg–Si–Cu–Zn alloy precipitate formation diagram. a) As quenched, b) short-term ageing, and c) Peak ageing. With permission from the cited source [88].

Table 9 – The experimental alloys' chemical composition (in weight%). Data were taken from Ref. [88].

Alloy	Mg	Si	Zn	Cu	Mn	Zr	Fe	Al
Zn-Free (#1 alloy)	0.90	0.82	0.006	0.23	0.11	0.09	<0.1	Bal.
Zn-Containing (#2alloy)	0.92	0.78	0.64	0.23	0.10	0.12	<0.1	Bal.

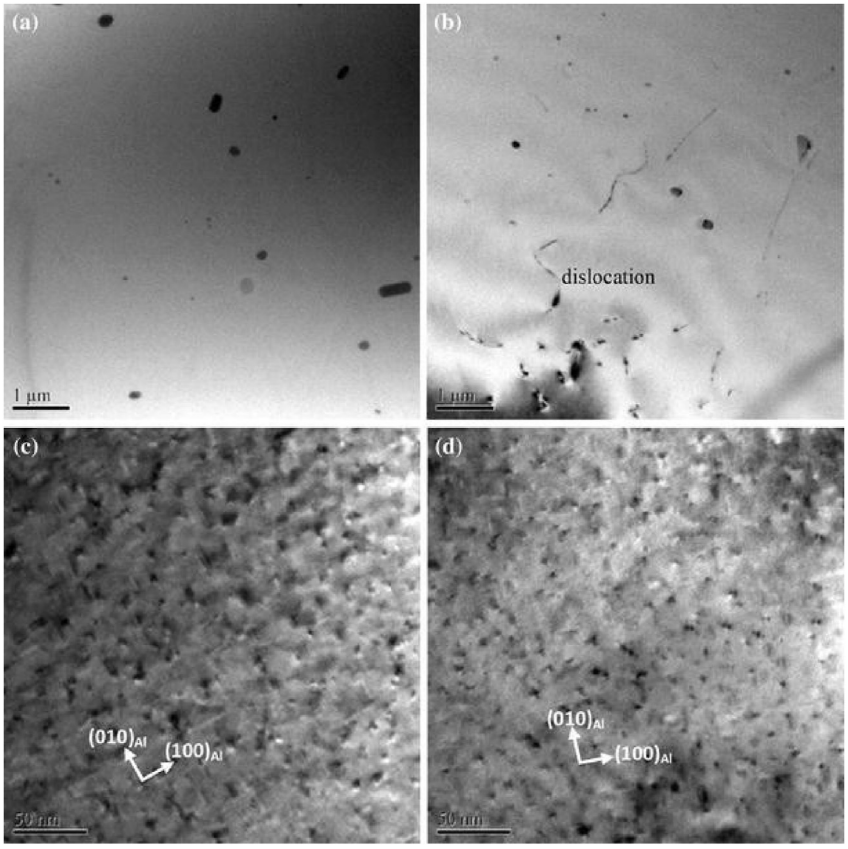

Fig. 28 – TEM and HRTEM microstructure are two alloys under different conditions. (a) As quenched of #1 alloy, (b) As quenched of #2 alloy, (c) 185 °C for 20 min #1 alloy, (d) 185 °C for 20 min #2 alloy. Adapted with permission from Ref. [88]. Consequences of zinc additions (up to 1 wt.%), the structure of precipitate, and intergranular corrosion was examined. The alloys demonstrated minor improvements in hardness after ageing at 185 °C as a function of Zn concentration. There were no Al–Zn–Mg alloy precipitates discovered. With permission from the cited source [88].

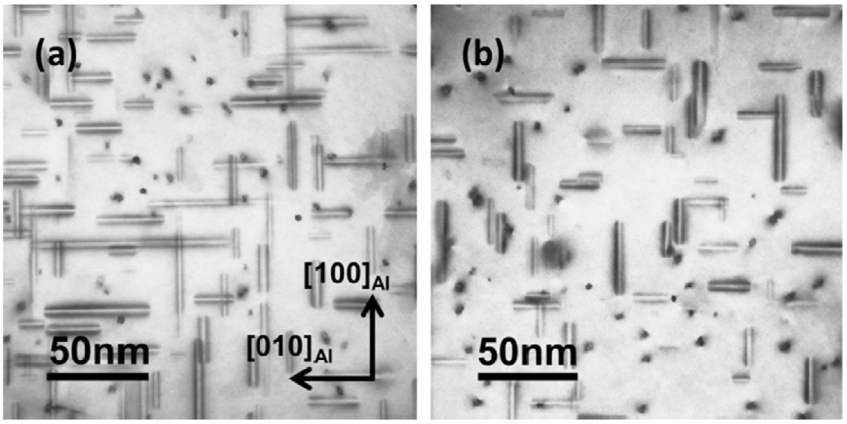

Fig. 29 – Bright-field TEM images of (a) LZ1(b) LZ4 after ageing at 185 °C for 12 h were taken along the <001>Al directions and have the same crystallographic orientation as (b). Cross-sections of the precipitation in the form of needles are shown as dark patches along the viewing direction. With permission from the cited source [78].

Table 10 – Combining alloy composition wt.% for the 5 alloys under investigation with predicted precipitate statics for the LZ1 and LZ4 alloys to create bright field TEM pictures. Data taken from Ref. [78].

Alloys	Al	Mg	Si	Zn	Number density (μm^{-3})	Volume fraction (%)
LZ0	Bal.	0.47	0.40	0.000	–	–
LZ1	Bal.	0.48	0.39	0.002	6397 ± 663	0.46 ± 0.02
LZ2	Bal.	0.47	0.40	0.012	–	–
LZ3	Bal.	0.48	0.41	0.110	–	–
LZ4	Bal.	0.47	0.39	1.019	7230 ± 792	0.49 ± 0.03

In heat-treatable 7xxx class (Al–Zn–Mg) aluminium alloys, Zn serves as the primary alloying element similar to the industrial alloy 7075, which frequently has 5.5 Zn, 2.5 Mg, and 1.5 Cu (wt.%). On 111 Al surfaces, Zn and Mg atoms interact to form equilibrium $MgZn_2$ precipitates and plate-like semi-coherent β′ metastable precipitates in this system [90].

The two alloys in Table 9 may have the same types of observed precipitates whereas alloy #2 had a higher strain hardening increment because the precipitates had different morphologies, which led to different strengthening contributions. The slightly higher precipitate density in the #2 alloy

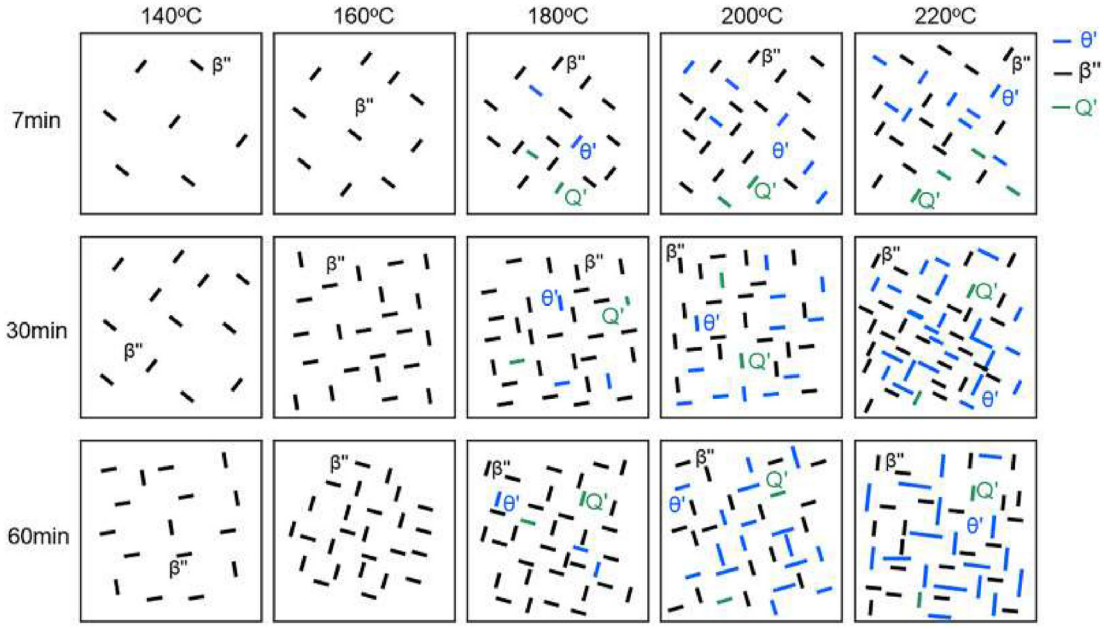

Fig. 30 – Schematic representation of the progression of the alloy's precipitation behaviour at various ageing temperatures. With permission from the cited source [91].

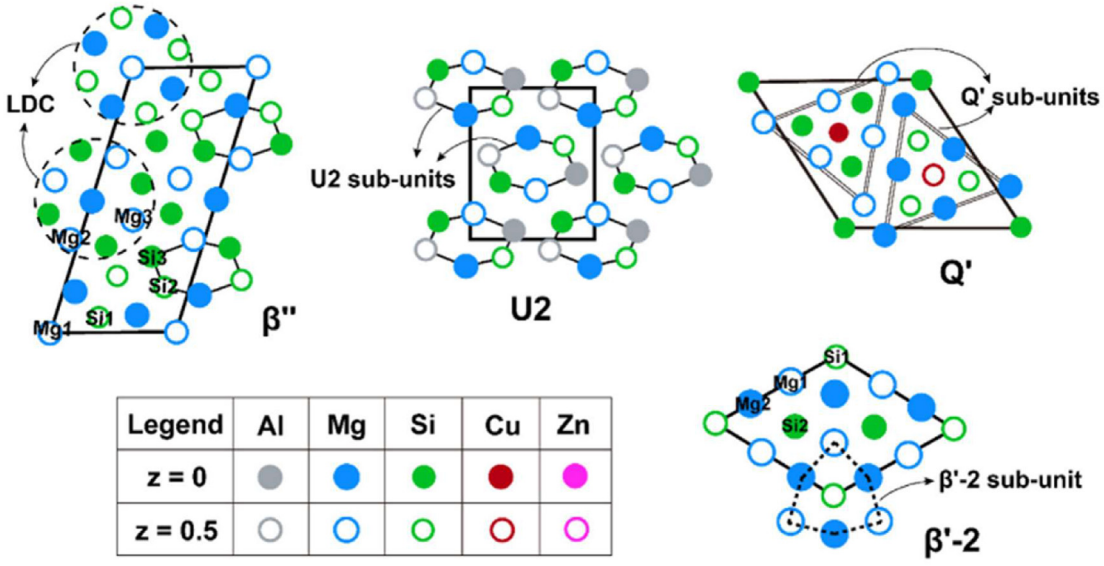

Fig. 31 – A schematic illustration of the β″, U2, Q′ and β′-2-unit cell. The four phases' distinctive sub units are denoted, respectively, by dashed line circles, sold-line hexagons, double-solid-line triangles, and hexagons with the triangle-like dash. Data taken from Ref. [92].

compared to alloy #1 is another contributing factor for the higher age-hardening jump produced in alloy #2 as seen in Fig. 28 [88].

Fig. 29 depicts bright-field TEM images of LZ1 and LZ4 in peak-aged conditions following a 12-h ageing process at 185 °C. Alloy composition shown in Table 10. This suggests that the examined alloys did not form η′ or η phases. Al–Zn–Mg alloys have lower typical ageing temperatures (120 °C), which should be mentioned. Mg prefers to interact with Si to produce precipitates that resemble needles for the heat treatment and composition described in this work rather than Zn. The key distinction between LZ1 and LZ4 is that LZ4 has a little greater precipitate number density [78].

If Al-9.02%Si-1.95%Cu-0.86%Mg-1.04%Zn-0.12%Fe-0.41% Mn is the measured alloy composition (in weight percent). As shown in Fig. 30, the alloy's hardness is effectively and significantly increased by 26.1% during artificial ageing at 220 °C for 30 min. The results of the hardness variation analysis demonstrate that when aged at low temperatures for a brief period of time, the HPDC (High-Pressure Die Casting) Al–Si–Cu–Mg–Mn–Zn alloys can significantly undergo an age-hardening reaction. It should be noted that ageing at 220 °C for 30 min results in the highest precipitate number density. This corresponds to the peaking-ageing condition Shown in Fig. 30 [91].

Fig. 31 provides a schematic drawing of the unit cells of the encountered known phases to make image analysis easier. It should be noted that the structure portions are enclosed by circles, hexagons, triangles, and triangle-like hexagons, respectively, which represent the characteristic sub-unit of β″, U2, Q′ and β′ [92] (see Fig. 32) [57].

2.1.3.2. *Mechanical properties*. In a study comparing the effects of Zn on the hardness of Al–Mg–Si alloys, the 0Zn alloy had an initial hardness of 61.7 HV, while the 3.5Zn alloy registered at 77.3 HV. With just 0.5 h of ageing, the hardness of the 3.5Zn alloy surged by 30.9%–101.2 HV, whereas the 0Zn variant saw a more modest increase of 14.3%–70.5 HV [57]. Peak hardness values also exhibited growth with Zn addition, showing an

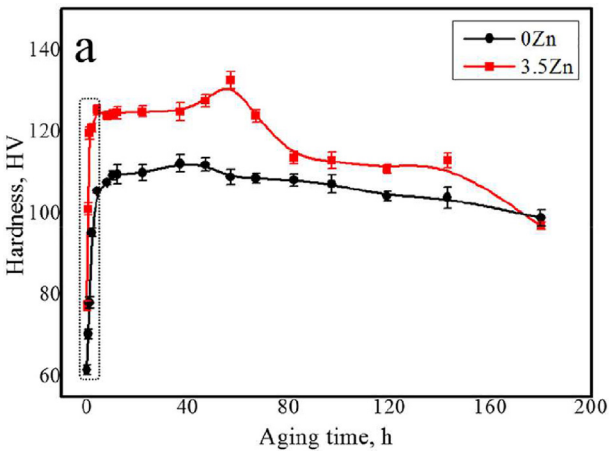

Fig. 32 – (a) 0Zn and 3.5Zn alloy age hardening curves. Data taken from Ref. [57].

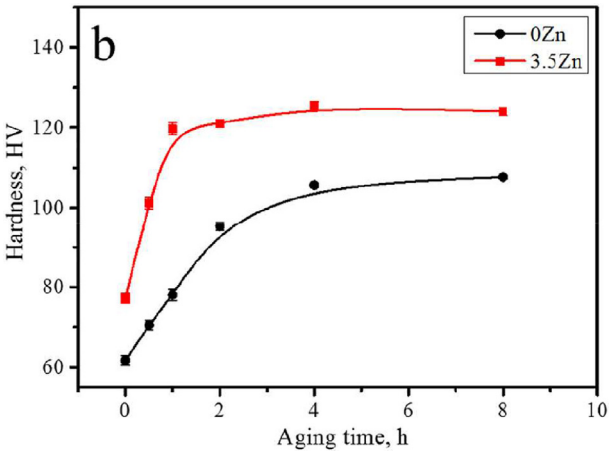

Fig. 33 – (b) 0Zn and 3.5Zn alloy enlarged curves at the early ageing stage. Data taken from Ref. [57].

18.2% increase from 112.3 HV to 132.7 HV, as depicted in Fig. 33. Furthermore, when comparing two alloys - one Zn-free and the other Zn-containing - the latter consistently demonstrated superior hardness throughout the ageing process (Fig. 34). This underscores Zn's efficacy in enhancing the age-hardening response in Al–Mg–Si alloys [92].

Fig. 35 (a) illustrates age hardening curves, with T6I6 showing higher hardness after 8 h at 170 °C, and pre-SR (Symmetry rolling) and pre-ASR (Asymmetry rolling) specimens becoming significantly harder than T6 and T6I6. However, pre-SR and pre-ASR specimens have lower thermal stability [93].

Fig. 35(b and c) presents tensile properties. T6I6 has higher UTS, YS, and El than T6. Pre-SR and pre-ASR specimens enhance strength but reduce elongation compared to T6, with pre-ASR having the highest strength. Summary, T6I6 improves strength and elongation compared to T6. Pre-rolling (SR and ASR) significantly boosts strength but reduces elongation. ASR

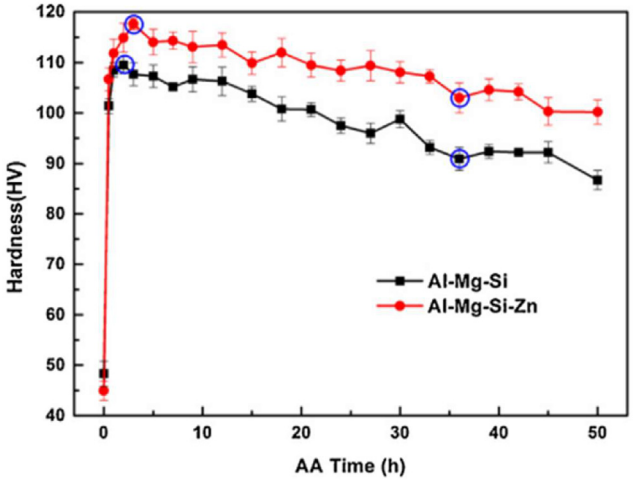

Fig. 34 – Age-hardening curves of the two alloys under investigation aged at 180 °C for various amounts of time. Data taken from Ref. [92].

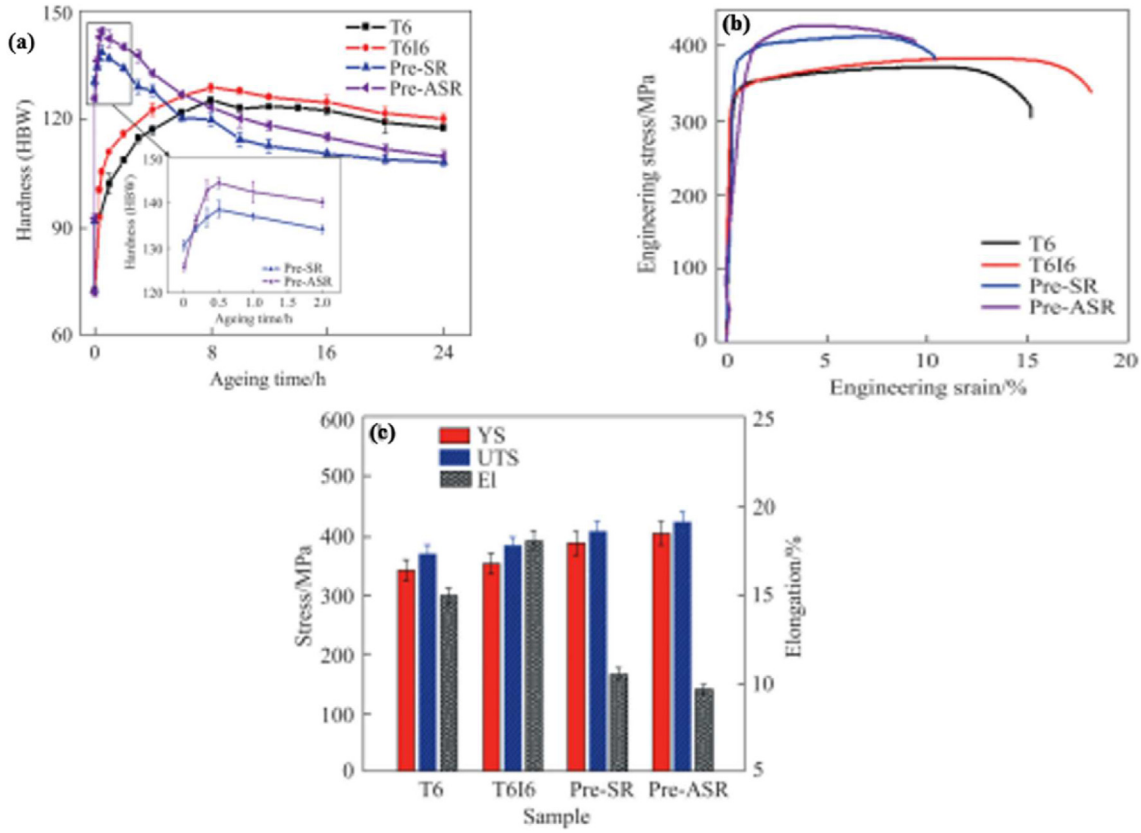

Fig. 35 – (a) Age hardening curves of alloy under different ageing regimes, Tensile properties of alloy at peak ageing under different ageing regimes: (b) Stress-strain curves; (c) Yield strength, ultimate tensile strength and elongation [93].

Table 11 – Precipitate phases seen in Al–Mg–Si alloys containing Ag.

Phases	Chemical Composition	Space groups	Lattice Parameters
β′[161]	$Al_3Mg_3Si_2Ag$	P62 m	$a = b = 0.6900$, $c = 0.4050$, $\gamma = 120.0°$
Q'_{Ag} [162]	$Mg_9Si_7Ag_2Al_3$		a = b = 1.0320 nm, c = 0.4050 nm, $\gamma = 120.0°$

has a more pronounced impact on strength enhancement and slightly lowers elongation compared to SR [93].

2.1.4. *Silver (Ag)*

2.1.4.1. *Microstructural analysis*. The supersaturated solid solution is represented by SSSS. Early in ageing, coherent with the Al-matrix, clusters and GP zones are produced. The strengthening phase in peak ageing is thought to be structured like a needle in β″ phase. It has been determined that β″ is made up of $Mg_5Al_2Si_4$ [94,95]. In earlier studies, this structural component was known as a low-density cylinder [34,41].

In Al–Mg–Si alloys, it is known that adding Cu or Ag improves precipitation strengthening [27,69,96,97]. The 6xxx AA properties, age-hardening response, and hardening kinetics may be significantly improved by Ag in comparison to Cu while also ensuring a very low strength in T4 temper. The formulation achieves a satisfactory balance between bake hardening and formability [98–100]. When Al–Mg–Si alloys are young, Ag aids in the formation of clusters. High cluster density causes the β″ phase to be denser and more evenly distributed, increasing the alloy's peak hardness [101].

The schematic illustration of Ag segregation on the morphology evolution of precipitate drawn in Table 11 is showed with the help of Fig. 36 given below (see Table 12) [22].

The quaternary Mg–Si–Ag–Al phase, with a hexagonal crystal structure and varying Mg:Si:Ag ratios, plays a role in aluminum alloys. The impact of silver (Ag) on crystal structures during initial aging and the formation of β'Ag and Q'Ag phases during excessive aging remains unclear [22]. Understanding Ag's influence on different precipitates in Al–Mg–Si

Table 12 – Symbolic representation of overlay of elements. Data were taken from Ref. [22].

Elements	Al	Si	Mg	Ag/Al
Z = 0.000 nm	○	○	○	○
Z = 0.203 nm	○	●	●	●

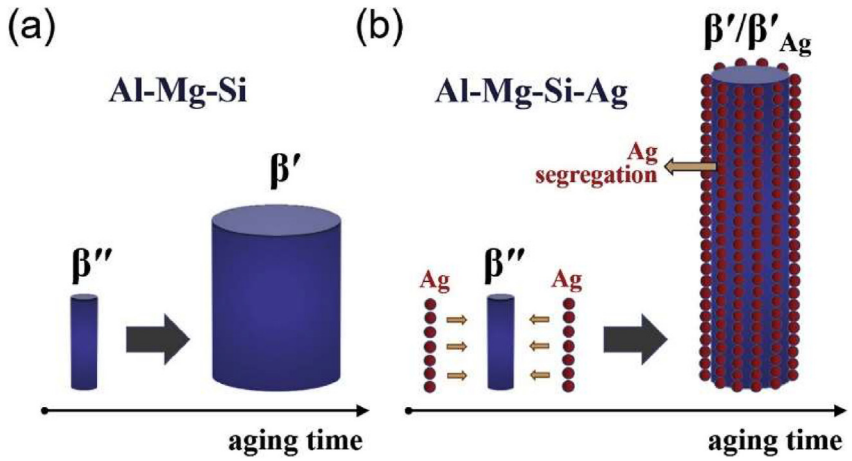

Fig. 36 – Diagram showing the development the morphology of precipitates in the 2 alloys under study: (a) the base Al–Mg–Si alloy and (b) the Al–Mg–Si–Ag alloy. With permission from the cited source [102].

alloys is crucial for enhancing alloy properties. Additionally, Ag can segregate at precipitate interfaces. Fig. 37 illustrates the Q′/C-like phase based on TEM observations and DFT calculations [22].

TEM characterisation was used to ascertain how the addition of Ag affected the microstructure of 6xxx AA [102]. Fig. 38 shows representative Precipitation TEM bright-field micrographs taken at various intervals during AA in the two alloys at 170 °C (2 h, 5 h, 2 days, and 1 week) [102]. The volume percentage and number density of precipitate in the A2 alloy with added Ag were found to be higher than those in the A1 base alloy at the peak-aged and over-aged stages, indicating that the addition of Ag may have aided in the development of precipitates [102].

2.1.4.2. *Mechanical properties*. The study focused on the Ag-added 6063 aluminium alloy. Using the 6063 commercial aluminium alloy as a base, it was melted and enriched with 99.98% pure silver in an argon-filled furnace. The melt was cast into a steel mould at room temperature [103]. Fig. 39(a) displays the Vickers microhardness evolution of both the base and Ag-added alloys. Both exhibited similar microhardness trends: an initial rise with ageing, peaking during under-ageing, and then decreasing during over-ageing [103].

Fig. 40 illustrates the hardness progression of the two alloys aged at 170 °C post-water quenching. Both alloys, as detailed in Table 13, showed a swift climb to peak hardness followed by a gradual decline. The Ag-added A2 alloy reached peak hardness faster and displayed higher overall hardness than the A1 base alloy [102].

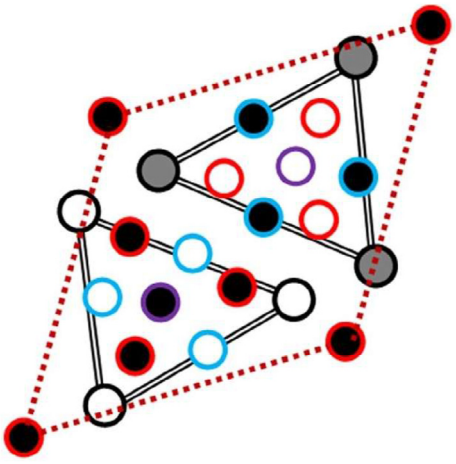

Fig. 37 – The site near the Centre of the double-lined triangles in the model of the Q′/C-like arrangements is occupied by Ag. Symbols similar to Table 9. With permission from the cited source [22].

3. Recycled materials have to be in 6XXX alloys designed for use in cars and electronics devices

Production of 6xxx series from scrap is still a challenge which could be understand from the figure shown below Fig. 41.

Due to the tendency of 20% of scrap from the 6xxx series is currently recycled into 6xxx wrought alloys, to contaminate recycled aluminium waste, Cu and Fe, or Zn and Mn, are the principal pollutants of concern in some alloys [104–106]. While most scrap streams contain only trace amounts of contaminants, some alloys have strict restrictions on metals like Cr which are minor alloying elements. Rolled, extruded, drawn, and forged 6xxx alloys find widespread use in a variety of industries, including construction, automotive, marine, and aerospace [107]. Fig. 42 demonstrates the variety of 6xxx series alloys, revealing that the only constraints that can't be met in the domain of wrought aluminium alloys are those of high strength and elongation [108].

The 6xxx alloy 6061 is ideal for reuse and recycling. The alloy's high absorption rates for Mg, Si, Fe, and Cu are mostly too responsible for this (see Table 14) [110,111]. It's a popular 6xxx alloy that sees a lot of use. There are other alloys in the 6xxx series that have much lower impurity tolerance levels. Alloys in the 6xxx series, like as 6022, are ideal for usage as automotive body sheets (ABS).

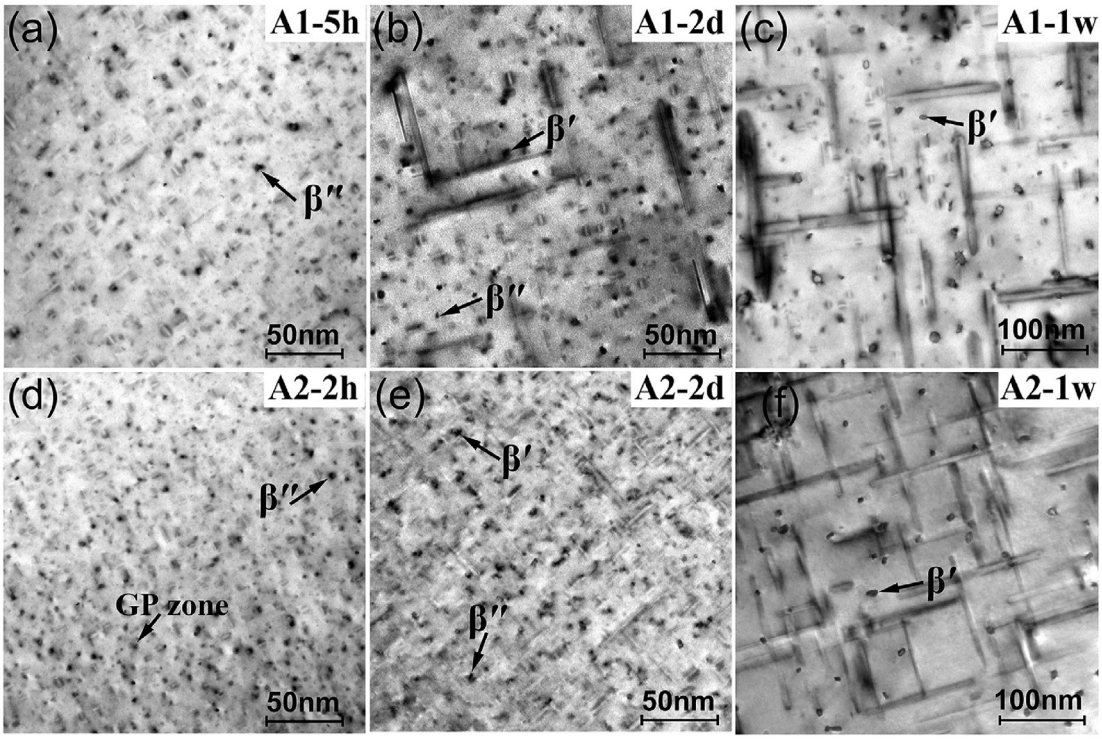

Fig. 38 – TEM bright-field pictures of the two alloys at various ageing temperatures of 170 °C. (a) A1, 5-h peak ageing, (b) A1, 2days AA, (c) A1, 1 week AA, (d) A2, 2-h peak ageing, (e) A2, 2days AA, and A2, (f) 1 week AA are examples of ageing patterns. With permission from the cited source [102].

Even the impurity-tolerant alloy 6061 may need significant dilution with primary aluminium if it is produced by recycling waste, according to a plot of dilution-quality-losses for 6061 made using a Monte Carlo-based decision support tool (Fig. 43) [111].

This is true even if high-quality scrap from automotive wrought aluminium (SC2) is used. Primary aluminium is in high demand if a scrap of lower quality is used. This includes scrap from engines and transmissions (SC1) and used beverage cans (UBC) (SC3). Adding other types of scrap metal

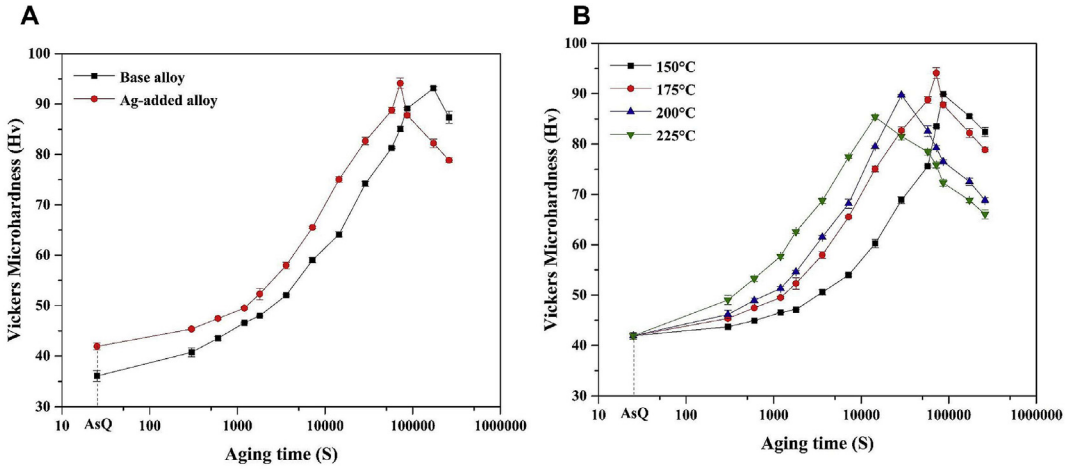

Fig. 39 – (a) As a function of ageing time at 175 °C, the base and Ag-added alloys' Vickers microhardness evolved. (b) Variations in the Ag-added alloy's Vickers microhardness as a function of ageing time at various temperatures. With permission from the cited source [103].

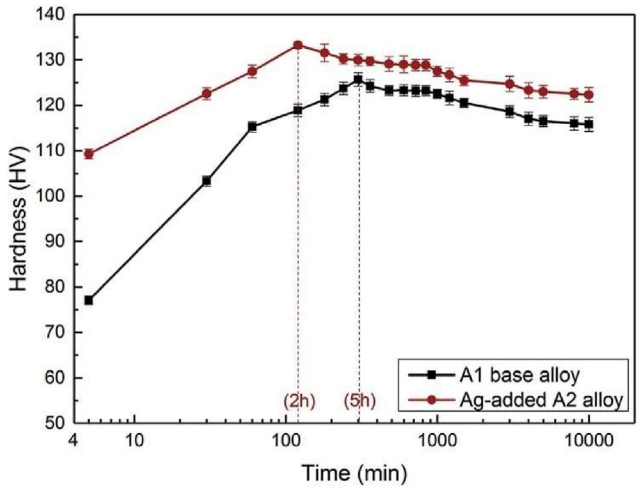

Fig. 40 – Change in Vickers hardness following water quenching for the two alloys under investigation during AA at 170 °C. With permission from the cited source [102].

Table 13 – The two alloys under investigation chemical compositions. Data taken from Ref. [102].

Alloy		Mg	Si	Fe	Mn	Ag
A1	Wt.%	1.090	0.710	0.110	0.060	–
A2	Wt.%	1.130	0.710	0.110	0.060	0.120

helps, but does not resolve the issue. As this illustration indicates, it is currently difficult to recycle old wrought alloys into brand-new 6xxx-series wrought alloys.

In conclusion, several cutting-edge recycling-based ideas for 6xxx alloys have been discussed in the most recent scholarly works. Kotadia et al. investigated adding more tramp elements to the present composition limits of 6xxx alloys, especially for Si, Fe, and Mg [106]. First, they demonstrated that ultrasonication during casting can efficiently change Fe-containing intermetallic compounds by refining grain structure and increasing homogeneity. Spray forming is one of the emerging technologies being explored to create feedstock for forming operations that can withstand a greater Fe content. As Pereira et al. demonstrated for wrought alloy 6061, undesirable IMCs (Intermetallic inclusions) may be prevented at 1.4 wt.% Fe [110]. In conclusion, the current literature emphasises the necessity of tolerating increased Fe contamination in the development of recyclable 6xxx series alloys. This includes research on non-traditional casting methods like alloy solidification, heat treatments, and solidification and inoculation.

4. Mechanical properties prediction using simulation

AMAP (Arctic Monitoring Assessment Programme) and other modelling techniques can be used to compare the alloy's mechanical properties, such as its ultimate tensile strength, hardness and yield strength [108]. The maximum yield strength predicted by the AMAP model is affected by the alloy composition (Alloy1-AMAP, Alloy2-AMAP) as shown in Fig. 44. Table 15 displays the alloy's composition. AMAP Model made the prediction of maximum yield strength (shown in Fig. 42, EXP Alloy1, EXP Alloy2) [112]) are typically closer to experimental data.

Cast Al–Mg–Si alloys containing 0.02, 0.73, and 3.72 wt.% Zn see increases of 72%, 44%, and 35% in yield strength and 57%, 48%, and 28% in tensile strength, respectively, when subjected to the optimal heat treatment conditions obtained using the CALPHAD (Calculation of phase diagram) technique which is shown in Fig. 45 [113].

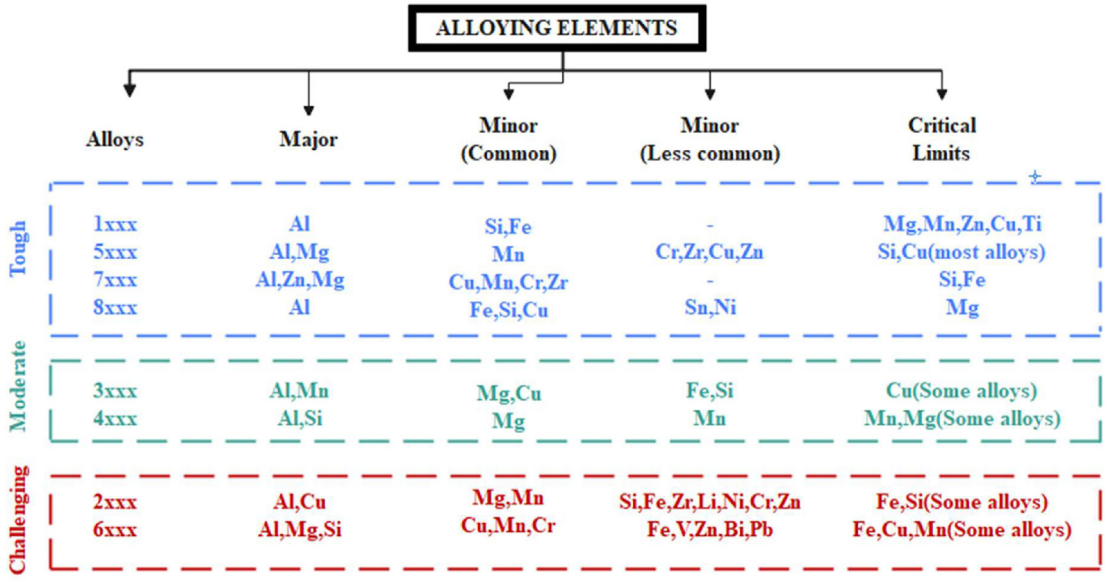

Fig. 41 – Critical limits for alloying components in wrought aluminium alloys.

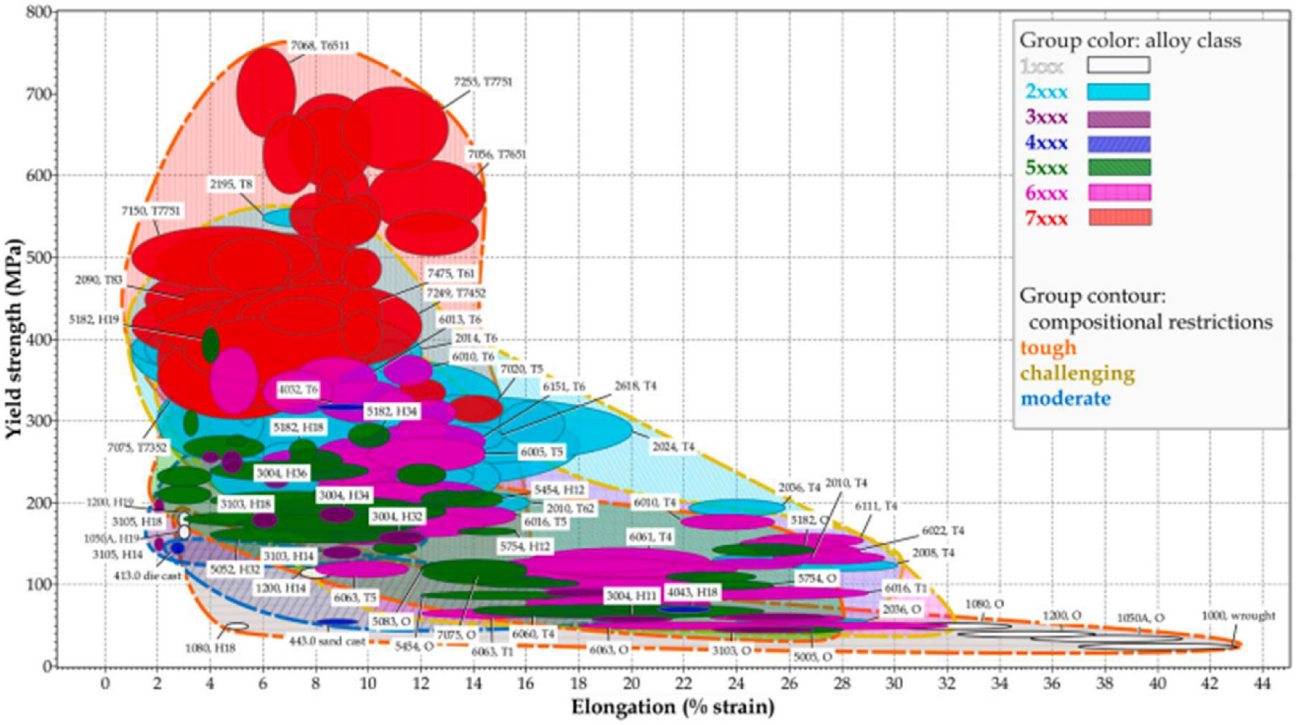

Fig. 42 – Wrought aluminium alloys 1xxx to 8xxx are compared in terms of their tensile strength. Fig. 38 depicts the study of where and how sensitive alloy attributes are to contamination by tramp elements [109].

Fig. 46 displays hardness measurement data used to verify the accuracy of the model calculations [41]. In contrast to the 0.2 J/m2 used in a more recent article and the 0.1 J/m^2 used in a number of different publications, Myhr's simulation uses an interfacial energy of 0.26 J/m^2. It's a miniature version of the bigger problems with nucleation modelling.

Myhr et al. recently proposed an age-hardening model for 6xxx AA that took into account the effect of protracted room-temperature storage and cold deformation on the alloy's reaction to artificial ageing [115]. The approach was also used to the characterization of metastable clusters, as well as their precipitations and phase transitions.

Table 14 – Typical 6xxx wrought alloy compositions and applications [109].

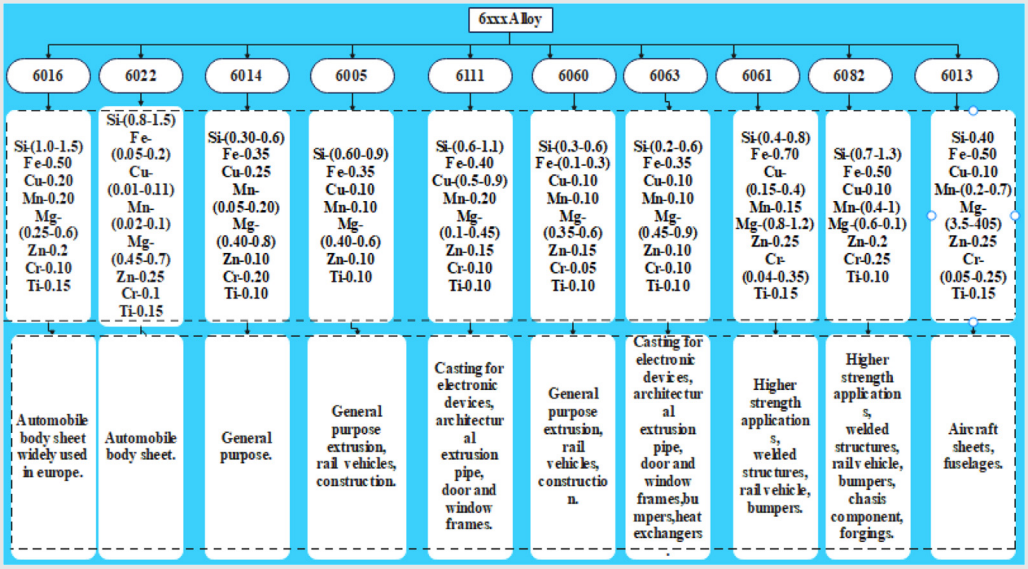

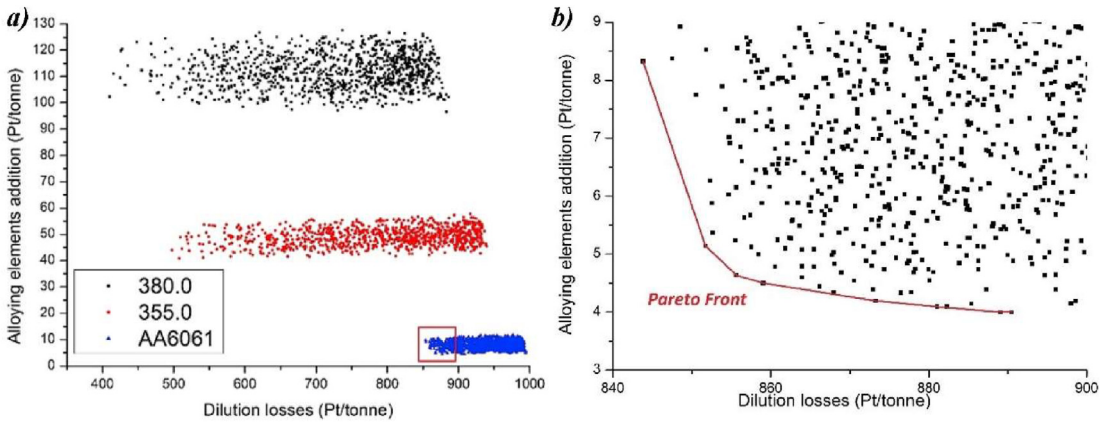

Fig. 43 – (a) Maximum scrap absorption solutions for the production of AA6061, 355.0, and 380.0 alloys (represented by red boxes in Fig. 42 a); (b) Magnification of the model's workable solution using SC3 (UBC scrap), alloying element and primary aluminium. The Pareto frontier is represented by a red line. With permission from the cited source [111].

Up-quenching (rapid heating combined with water quenching) vacancy development thermo-kinetic simulations were performed in MatCalc (Material Calculator) 6.0025 [116,117]. The Fischer Svoboda Appel kozeschnik (FSAK) model can be used to predict both the generation and annihilation of structural vacancies for idealised microstructural sources like grain boundaries and dislocation jogs [118].

They simulate the precipitation process by modifying the multi-phase, multi-component Kampmann-Wagner Numerical framework described in Ref. [119]. The KWN method takes into account particle interactions by means of the mean-field concept based on the growth, coarsening and classical nucleation rules. The fundamental premise of this approach is that similar precipitates can be connected to different size classes on the precipitate size distribution curve [34]. The KWN model predicts the nucleation, growth, and coarsening of microstructures during welding processes, typically for spherical precipitates. In Al–Mg–Si alloys, needle-like precipitations are characterized by a shape factor representing their length-to-tip radius ratio, improving calculation accuracy. However, for alloys like the 6XXX series with high aspect ratios, this isn't always accurate. Key assumptions include neglecting elastic energy, considering only homogeneous nucleation, simplifying to a single precipitate type (Mg_xSi_y), and describing needle-shaped precipitates as a cylinder with hemispheres at both ends. Precipitate size distribution is visualized in Fig. 47, detailing the evolution of Ni and ri.

In Al–Mg–Si alloys, precipitation is represented by a shape factor based on the length and tip radius of needle-like structures, enhancing calculation accuracy. The current numerical model is apt for calculating precipitation kinetics in the heat-affected zone (HAZ) or wrought sheet of welded aluminium alloy [121]. However, it's unsuitable for the fusion zone due to its microscopically varied solute distribution. To fully comprehend weld microstructural evolution, a model accounting for micro-segregation is essential [121].

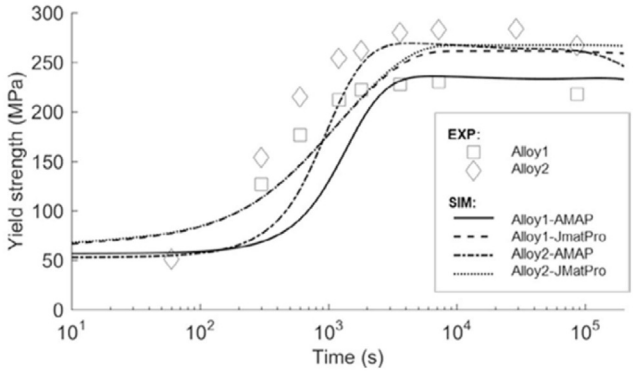

Fig. 44 – The AMAP model's forecasts for the change in yield strength during artificial ageing as a function of alloy composition. The outcomes were compared to those of a popular commercial programme. With permission from the cited source [112].

5. Future scope

NA is the main problem which researchers were facing while using 6xxx AA and this effect can be minimised by adding foreign element into it. Therefore, various elements have been chosen from the periodic table which can be added in 6xxx AA

Table 15 – Composition of alloy 1 and alloy 2.

Alloy Name	Content Mg	Content Si	Content Cu	Content others
Alloy 1	0.3	1.330	<0.003	<0.2
Alloy 2	0.455	1.059	0.037	<0.225

A vital lightweight material, hypoeutectic (12 wt.% Si) Al–Si–Mg alloys have a number of advantageous traits, such as a high strength-to-weight ratio, superior cast-ability, mechanical qualities, recyclability, and excellent corrosion resistance. As a result, it is widely used to make large casts with sophisticated structures for the transportation industry, including chassis frames and housings for battery module housings for electric cars [2,3].

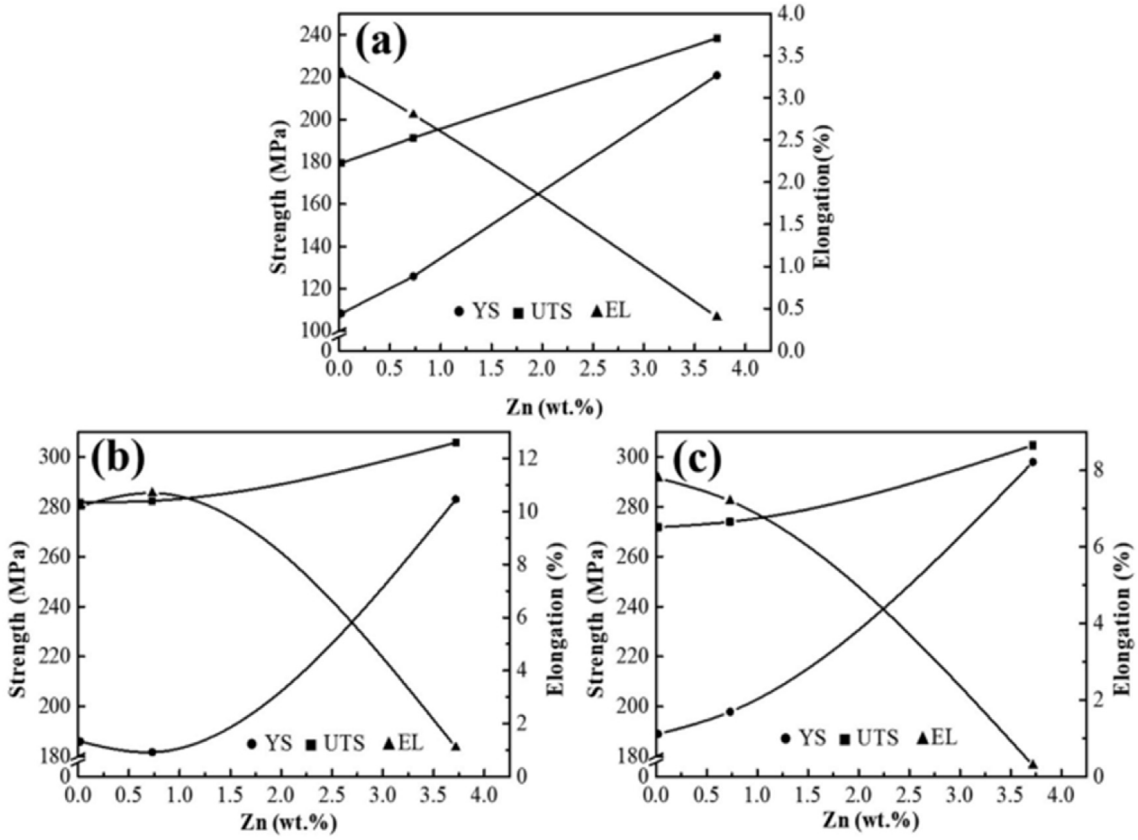

Fig. 45 – At 120 °C, the tensile characteristics of the three cast alloys are as follows: There are three sets of tensile properties to consider: (a) as-cast tensile properties; (b) first peak ageing tensile properties at 120 °C; and (c) second peak ageing tensile properties at 120 °C. With permission from the cited source [113].

but still very less element has been papers published on this. Various element on which very less research has been done is shown below.

- The impact of Au, Co [65], and Ni on the atomic structure of precipitate which formed in the Al–Mg–Si system has not yet been thoroughly studied. In general, these elements are poorly soluble in aluminium as solids. To the extent that these elements are included in precipitates, a number of observations can be made.
- No novel precipitate forms have been discovered in alloys containing Ni, Co, or Au [30]. These substances, however,

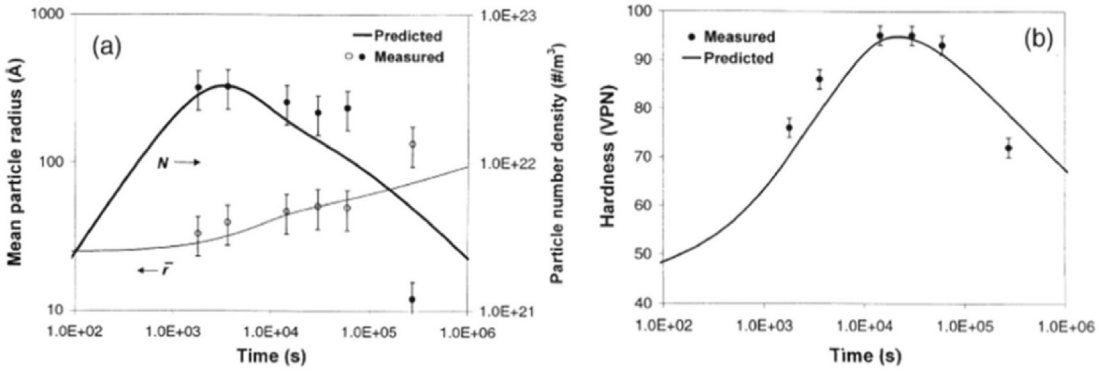

Fig. 46 – AA6005 alloy's expected and observed behaviour after artificial ageing at 185 °C. (a) time-dependent changes in particle density (N) and mean particle radius (r). (b) Change in hardness after quenching to room temperature as a function of time [114].

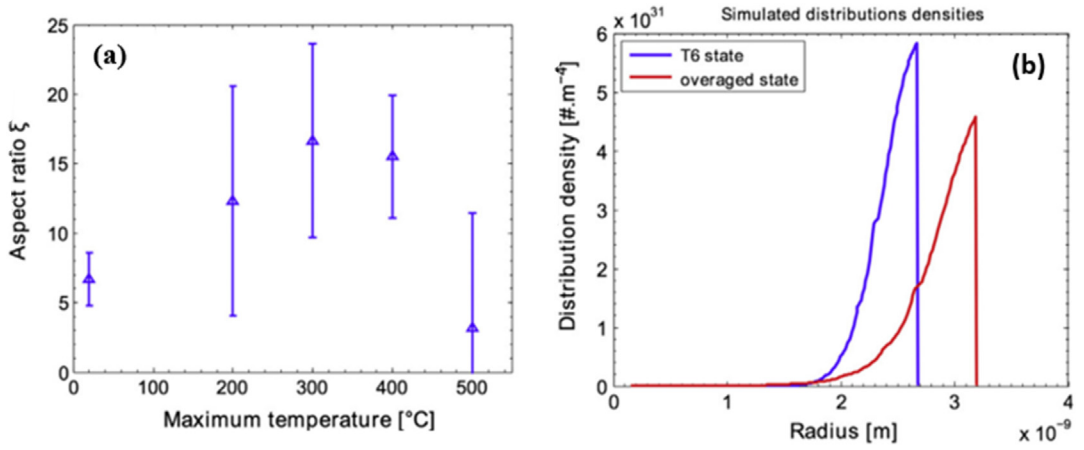

Fig. 47 – (a) Aspect ratio $1/r_p$ from SANS fitting. The error bar is the standard deviation given by the fitting on several samples that have been the same temperature treatment, (b) Precipitate distribution density for a state that is overaged and in the T6 stage. With permission from the cited source [120].

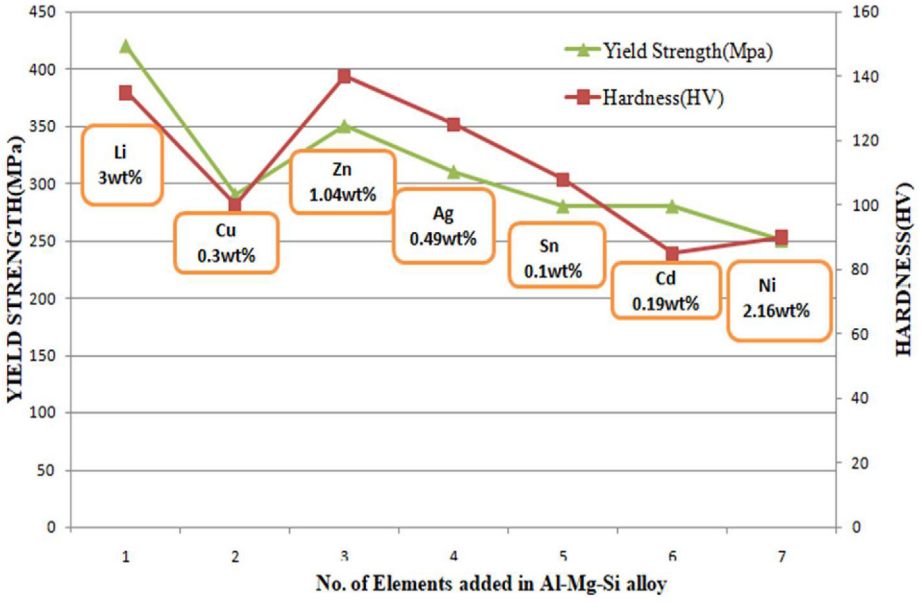

Fig. 48 – Yield Strength and Hardness of various elements that are added in 6xxx AA at the respective weight percent.

are more frequently detected near the interface of precipitate/matrix and either reside there.

- Co's impact on the precipitate formations is minimal. At the interface of "precipitates" that are too old, Co atoms can be seen. At the interface of 'precipitates in an old state, Au atoms are present. Little addition of Sn in 6xxx AA occupies its vacancies during natural ageing [122].
- Fig. 48 signifies the yield strength and hardness of various elements that can be added to Al–Mg–Si alloys. This data can help improve the mechanical properties of 6xxx series Aluminium alloys at different weights percent.

If we improve the quality of 6xxx series AA alloy by adding these elements, it not only helps industries to improve its product quality for various application but also help researchers to do a novel work which could benefit the society.

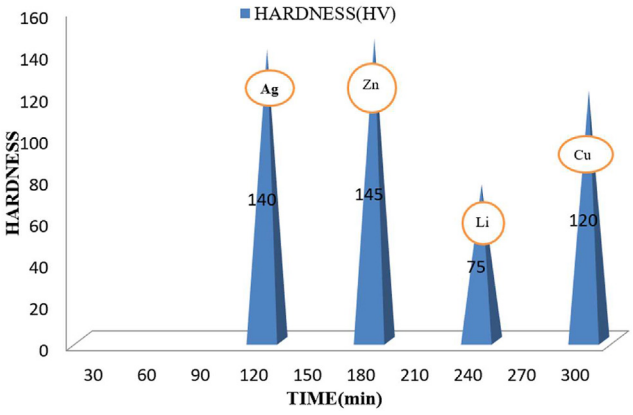

Fig. 49 – Hardness of the foreign elements which are added in 6xxx AA.

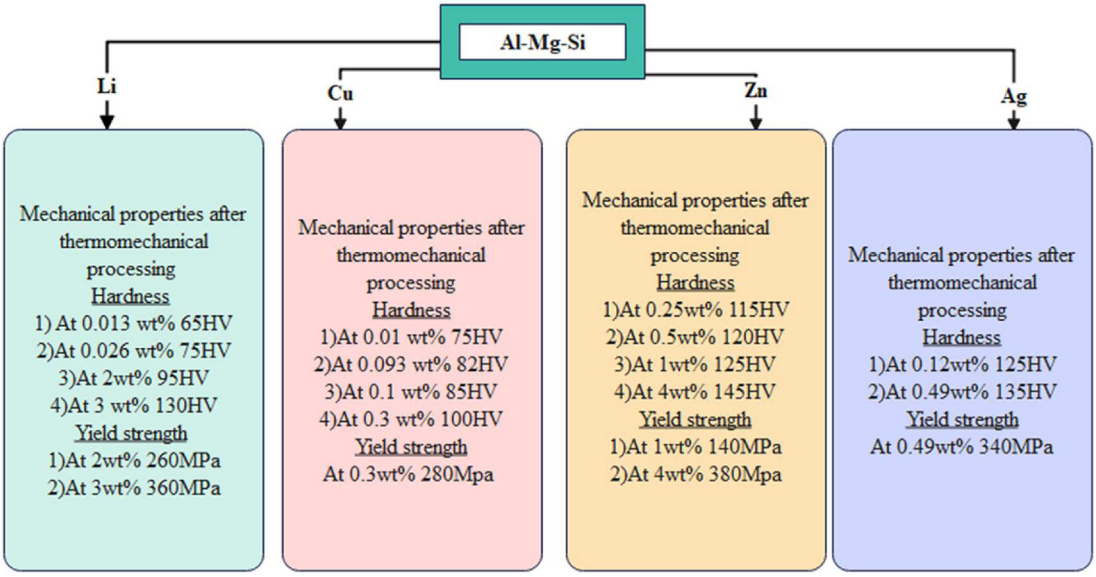

Fig. 50 – Mechanical properties which are obtain after thermomechanical processing by the addition of various element in 6xxx AA at different weight percent.

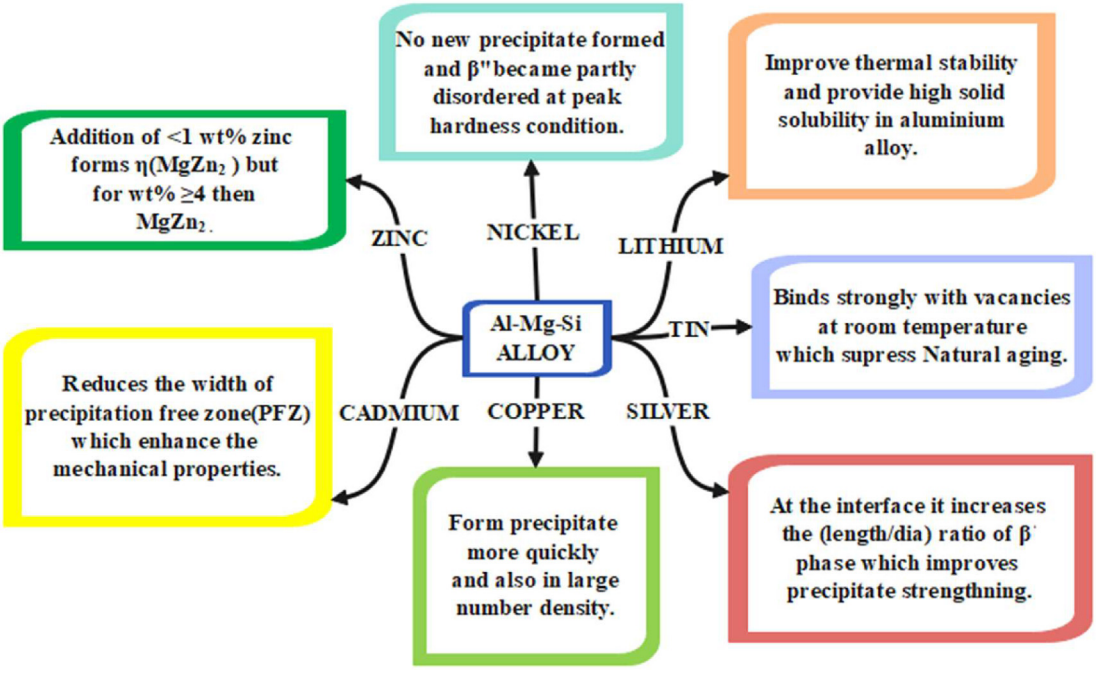

Fig. 51 – Change in the properties by adding different foreign elements in the 6xxx AA.

6. Conclusions

The mechanical characteristics and microstructure of the precipitates are significantly impacted by the participation of different elements in the addition of 6xxx AA. The strength of age-hardenable 6xxx AA is essentially reduced by the nano-scale precipitates that develop during natural ageing. Therefore, it is crucial to reduce NA's negative effects and enhance the age hardening of 6xxx AA. The additional component greatly enhanced the mechanical properties, suppressed NA, and disorganised the original microstructure. The following is a list of the conclusions drawn from the work described:

- When Li is added to 6xxx it occupies Mg3 sites in the β″ phase which is proved by density functional theory (DFT) in various research papers. Li addition in 6xxx AA enhances the

precipitate sizes and density which improved the hardness compared to the conventional 6xxx AA by doing solutioning of Li added to 6xxx AA at the artificially aged at 195 °C for 4hrs the hardness is nearly 75HV as shown in Fig. 49.

- Cu changes the precipitation sequences in 6xxx AA and produces a variety of precipitates, including L, C, QP, and QC at the peak of ageing and Q′ during the over-aging stage. DFT simulations indicate that the Si3/Al site is most conducive to Cu inclusion in β″. 6xxx AA with Cu has a harder surface than 6xxx AA without Cu because large amounts of Cu produce the highest volume fraction of precipitates. When Cu is added to 6xxx AA and they are solution aged at 190 °C for 5 h, as shown in Fig. 49, the hardness is close to 120HV.
- There is no possibility of the η′ phase forming when Zn concentration (1.0 wt.%) is added to 6xxx AA. The amount of Zn in the 6xxx AA directly relates to their hardness. By solutioning Zn-added Al–Mg–Si alloys at 220 °C for 30 min during artificial ageing, as shown in Fig. 49, Zn influences the formation of a precipitate that raises the hardness to 145HV.
- Ag helps to form an alloy of Al–Mg–Si clusters during the start of ageing which results in an orientation of finer and denser β″ phase, which raises the alloy's peak hardness and its own precipitate type is formed i.e., β'_{Ag} The segregation of these phases in metastable phases leads to improve hardness to 140HV by doing solutioning of Ag added in 6xxx AA at the artificial ageing of 170 °C for 2 h as shown in Fig. 49.

The conclusion of the whole paper related to the mechanical properties after thermomechanical processing is describe in Fig. 50. Whereas Fig. 51 describe the change in the properties and precipitate behaviour of the 6xxx AA when the addition of foreign element done in it.

Zn has been found to be one of the best added elements for 6xxx AA when compared to all the other added elements, showing 135 HV after artificial ageing for 30 min at 220 °C. 6xxx AA with Zn tend to have more conventional precipitates present, which contributes to the alloys' increased strength. When compared to the other three elements, Zn was found to be more economical.

Data availability

The raw/processed data required to reproduce these findings cannot be shared at this time as the data also forms part of an ongoing study.

Author contribution

Pallavi Singh: Conceptualization, Methodology, Resources, Writing- Original draft preparation., **D Atchuta Ramacharyulu:** Formal analysis, **Nikhil Kumar:** Supervision, Project administration, Writing - review & editing, Formal analysis; Funding acquisition, **Kuldeep K Saxena:** Review & editing, **Sayed M Eldin:** Data accumulation.

Data and code availability

Not applicable.

Ethical approval

Not applicable.

Declaration of competing interest

The authors declare that they have no known competing financial interests or personal relationships that could have appeared to influence the work reported in this paper.

Acknowledgement

The authors acknowledge the financial support from grant SERB-SRG/2022/000978.

REFERENCES

[1] Meinshausen M, Meinshausen N, Hare W, Raper SC, Frieler K, Knutti R, et al. Greenhouse-gas emission targets for limiting global warming to 2 degrees C. Nature 2009;458(7242):1158–62. https://doi.org/10.1038/nature08017. PMID: 19407799.
[2] Monthly energy review. 2021. www.eia.gov/mer.
[3] Kumar N. Investigation of tensile properties and microstructural evolution of Al–Mg–Si alloy produced through the multi-axial forging at −147 C and room temperature. Vacuum 2022;205:111471. https://doi.org/10.1016/J.VACUUM.2022.111471.
[4] Wolverton C. Crystal structure and stability of complex precipitate phases in Al-Cu-Mg-Si and Al-Zn-Mg alloys. Acta Mater 2001;49:3129–42.
[5] Ravi C, Wolverton C. First-principles study of crystal structure and stability of Al-Mg-Si-Cu precipitates. Acta Mater 2004;52:4123–227.
[6] Marioara CD, Andersen SJ, Jansen J, Zandbergen HW. Atomic model for GP-Zones in A 6082 Al-Mg-Si system. Acta Mater 2001;49:321–8.
[7] Van Huis MA, Chen JH, Zandbergen HW, Sluiter MHF. Phase stability and structural relations of Nanometer-sized matrix-embedded precipitate phases in Al-Mg-Si alloys in the late stages of evolution. Acta Mater 2006;54:2945–55.
[8] Ninive Per Harald, Strandlie Are, Gulbrandsen-Dahl Sverre, Lefebvre Williams, Marioara Calin D, Andersen Sigmund J, et al. Detailed atomistic insight into the β″ phase in Al-Mg-Si alloys. Acta Mater 2014;69:126–34.
[9] Ehlers FJH, Wenner S, Andersen SJ, Marioara CD, Lefebvre W, Boothroyd CB, et al. Phase stabilization principle and precipitate-host lattice influences for Al-Mg-Si-Cu alloy precipitates. J Mater Sci 2014;49:6413–26. https://doi.org/10.1007/s10853-014-8371-4.
[10] Saito Takeshi, Ehlers Flemming JH, Lefebvre Williams, Hernandez-Maldonado David, Bjorge Ruben, Marioara Calin D, et al. HAADF-STEM and DFT investigations of the Zn-

containing β″phase in Al-Mg-Si alloys. Acta Mater 2014;78:245–53.
[11] Lai YX, Jiang BC, Liu CH, Chen ZK, Wu CL, Chen JH. Low-alloy-correlated reversal of the precipitation sequence in Al-Mg-Si alloys. J Alloys Compd 2017;701:94–8.
[12] Li Kai, Armand Béché, Song Min, Sha Gang, Lu Xingxu, Zhang Kai, et al. Atomistic structure of Cu-containing β″ precipitates in an Al–Mg–Si–Cu alloy. Scripta Mater 2014;75:86–9.
[13] Itkis ME, Borondics F, Yu A, Haddon RC. Bolometric infrared photoresponse of suspended single-walled carbon nanotube films. Science 2006;312:413–6. https://doi.org/10.1126/science.1125695. 1979.
[14] Dieter G. Mechanical metallurgy. SI metric edition. London, UK: McGraw-Hill; 1988.
[15] Baruah Monoj, Borah Anil. Processing and precipitation strengthening of 6xxx series aluminium alloys: a review. international journal of material science 2020;1(1). https://doi.org/10.22271/27078221.2020.v1.i1a.10. Part A.
[16] Andersen SJ, Marioara CD, Vissers R, Froseth A, Zandbergen HW. The structure relation between precipitates in Al-Mg-Si alloys, the Al-matrix and diamond silicon, with emphasis on the trigonal phase U1-MgAl2Si2. Mater Sci Eng, A 2007;444:157–69.
[17] Andersen SJ, Marioara CD, Froseth A, Vissers R, Zandbergen HW. Crystal structure of the orthorhombic U2-Al4Mg4Si4 precipitate in the Al-Mg-Si alloy system and its relation to the β′, β″ phases. Mater Sci Eng, A 2005;390:127–38.
[18] Chen Haonan, Lu Jiangbo, Kong Yi, Li Kai, Tong Yang, Meingast Arno, et al. Atomic-scale investigation of the crystal structure and interfaces of the B′ precipitate in Al-Mg-Si alloys. Acta Mater 2020;185:193–203.
[19] Vissers R, van Huis MA, Jansen J, Zandbergen HW, Marioara CD, Andersen SJ. The crystal structure of the β′phase in Al-Mg-Si alloys. Acta Mater 2007;55:3815–23.
[20] Asghar G, Peng L, Fu P, Yuan L, Liy Y. Role of Mg2Si precipitates size in determining the ductility of A357 cast alloy. Mater Des 2020;186:108280.
[21] Davis JR. Aluminum and aluminum alloys. Materials Park, OH, USA: ASM Speciality Handbook, ASM International; 1993.
[22] Malekan A, Emamy M, Rassizadehghani J, Malekan M. Effect of isothermal holding on semisolid microstructure of Al-Mg_2Si composites. Int Sch Res Notices 2012. https://doi.org/10.5402/2012/631096. Article ID 631096.
[23] Serizawa A, Hirosawa S, Sato T. Three-Dimensional atom probe characterization of nanoclusters responsible for multistep aging behavior of an Al-Mg-Si alloy. Metall Mater Trans A Phys Metall Mater Sci 2008;39:243–51. https://doi.org/10.1007/s11661-007-9438-5.
[24] Qian Feng, Zhao Dongdong, Mørtsell Eva A, Jin Shenbao, Wang Junsheng, Marioara Calin D, et al. Enhanced nucleation and precipitation hardening in Al–Mg–Si(–Cu) alloys with minor Cd additions. Mater Sci Eng, A 2020:792.
[25] Liu Chunhui, Ma Peipei, Zhan Lihua, Huang Minghui, Li Jianjun. Solute Sn-induced formation of composite β′/β″ precipitates in Al-Mg-Si alloy. Scripta Mater 2018;155:68–72.
[26] Mørtsell EA, Marioara CD, Andersen SJ, Røyset J, Reiso O, Holmestad R. Effects of germanium, copper, and silver substitutions on hardness and microstructure in lean Al-Mg-Si alloys. Metall Mater Trans A Phys Metall Mater Sci 2015;46:4369–79. https://doi.org/10.1007/s11661-015-3039-5.
[27] Zandbergen MW, Cerezo A, Smith GDW. Study of precipitation in Al–Mg–Si Alloys by atom probe tomography II. Influence of Cu additions. Acta Mater 2015;101:149–58.
[28] Sunde Jonas K, Marioara Calin D, Holmestad Randi. The effect of low Cu additions on precipitate crystal structures in overaged Al-Mg-Si(-Cu) alloys. Mater Char 2020:160.
[29] Werinos M, Antrekowitsch H, Ebner T, Prillhofer R, Curtin WA, Uggowitzer PJ, et al. Design strategy for controlled natural aging in Al–Mg–Si alloys. Acta Mater 2016;118:296–305.
[30] Pogatscher S, Antrekowitsch H, Werinos M, Moszner F, Gerstl SSA, Francis MF, et al. Diffusion on demand to control precipitation aging: application to Al-Mg-Si alloys. Phys Rev Lett 2014;112. https://doi.org/10.1103/PhysRevLett.112.225701.
[31] Saito T, Mørtsell EA, Wenner S, Marioara CD, Andersen SJ, Friis J, et al. Atomic structures of precipitates in Al–Mg–Si alloys with small additions of other elements. Adv Eng Mater 2018;20. https://doi.org/10.1002/adem.201800125.
[32] Rometsch PA, Wang SC, Harriss A, Gregson PJ, Starink MJ. The effect of homogenizing on the quench sensitivity of 6082. 2002.
[33] Bratland DH, Grong O, Shercliff H, Myhr OR, Tjotta S. Modelling of precipitation reactions in industrial processing. Acta Mater 1997;45:1–22.
[34] Du Qiang, Jia Lina, Tang Kai, Holmedal Bjørn. Modelling and experimental validation of microstructure evolution during the cooling stage of homogenization heat treatment of Al-Mg-Si alloys. Materialia 2018;4:70–80.
[35] Strobel K, Easton MA, Sweet L, Couper MJ, Nie JF. Relating quench sensitivity to microstructure in 6000 series aluminium alloys. Mater Trans 2011:914–9. https://doi.org/10.2320/matertrans.L-MZ201111.
[36] Que Zhongping, Zhou Yipeng, Wang Yun, Mendis Chamini L, Fan Zhongyun. Effects of Mg addition on the Al6(Fn,Mn) intermetallic compounds and the grain refinement of α-Al in Al-Fe-Mn alloys. Mater Char 2021:171.
[37] Guo Y, Wei W, Shi W, Zhang B, Zhou X, Wen S, et al. Effect of Er and Zr additions and aging treatment on grain refinement of aluminum alloy fabricated by laser powder bed fusion. J Alloys Compd 2022;912. https://doi.org/10.1016/j.jallcom.2022.165237.
[38] Wang M Mantina Y, Chen LQ, Liu ZK, Wolverton C. First principles impurity diffusion coefficients. Ata Materialia 2009;57:4102–8.
[39] Du Yong, Chang YA, Huang Baiyun, Gong Weiping, Jin Zhanpeng, Xu Honghui, et al. Diffusion coefficients of some solutes in fcc and liquid Al: critical evaluation and correlation. Mater Sci Eng, A 2003;363:140–51.
[40] Zhang J, Fan Z, Wang YQ, Zhou BL. Equilibrium pseudobinary Al–Mg2Si phase diagram. Mater Sci Technol 2001;17(5):494–6.
[41] Tang Kai, Du Qiang, Li Yanjun. Modelling microstructure evolution during casting, homogenization and ageing heat treatment of Al-Mg-Si-Cu-Fe-Mn alloys. Calphad 2018;63:Pages164–184.
[42] Murayama Mitsuhiro, Hono Kazuhiro. PRE-PRECIPITATE clusters and precipitation processes. 1999.
[43] Hasting HS, Frøseth AG, Andersen SJ, Vissers R, Walmsley JC, Marioara CD, et al. Composition of B″ precipitates in Al-Mg-Si alloys by atom probe tomography and first principles calculations. J Appl Phys 2009;106. https://doi.org/10.1063/1.3269714.
[44] H.W. Zandbergen, " S J Andersen, J. Jansen, Structure determination of Mg5Si6 particles in Al by dynamic electron diffraction Studies, DOI:10.1126/SCIENCE.277.5330.1221.
[45] Andersen SJ, Zandbergen HW, Jansen J, TrÆholt C, Tundal U, Reiso O. The crystal structure of the β″ phase in Al–Mg–Si alloys. Acta Mater 1998;46:3283–98.
[46] do Nascimento AT, Claudio GK. Functional and radiological evaluation of acute acromioclavicular dislocation treated

with anchors without eyelet: comparison with other techniques. Revista Brasileira de Ortopedia (English Edition) 2016;51:561–8. https://doi.org/10.1016/j.rboe.2016.08.015.
[47] Tsao CS, Chen C-Y, Jeng U-S, Kuo T-Y. Precipitation kinetics and transformation of metastable phases in Al–Mg–Si alloys. Acta Mater 2006;54:4621–31.
[48] Marioara CD, Andersen SJ, Birkeland A, Holmestad R. Orientation of silicon particles in a binary Al-Si alloy. J Mater Sci 2008;43:4962–71. https://doi.org/10.1007/s10853-008-2730-y.
[49] Zandbergen HW, Andersen SJ, Jansen J. Structure determination of Mg$_5$Si$_6$ particles in Al by dynamic electron diffraction. 1997.
[50] Sha G, Möller H, Stumpf WE, Xia JH, Govender G, Ringer SP. Solute nanostructures and their strengthening effects in Al–7Si–0.6Mg alloy F357. Acta Mater 2012;60:692–701.
[51] Edwards GA, Stiller K, Dunlop GL, Couper MJ. The precipitation sequence in Al–Mg–Si alloys. Acta Mater 1998;46:3893–904.
[52] Pogatscher S, Antrekowitsch H, Leitner H, Sologubenko AS, Uggowitzer PJ. Influence of the thermal route on the peak-aged microstructures in an Al–Mg–Si aluminum alloy. Scripta Mater 2013;68:158–61.
[53] Liu Y, Lai YX, Chen ZQ, Chen SL, Gao P, Chen JH. Formation of β"-related composite precipitates in relation to the enhanced thermal stability of Sc-alloyed Al-Mg-Si alloys. Journal of alloys and compound 2021:885.
[54] Ding Lipeng, Chen Ji, Lu Chang, Zang Ruojin, Weng Yaoyao, Liu Qing, et al. Study of the precipitate evolution mechanism in an Al-Mg-Si-Cu alloy with Si-rich and low Cu composition. Mater Char 2022;191:112167.
[55] Mørtsell Eva A, Marioara Calin D, Andersen Sigmund J, Ringdalen Inga G, Jesper Friis, Wenner Sigurd, et al. The effects and behaviour of Li and Cu alloying agents in lean Al-Mg-Si alloys. J Alloys Compd 2017;699:235–42.
[56] Ehlers Flemming JH. Ab initio interface configuration determination for β″ in Al–Mg–Si: beyond the constraint of a preserved precipitate stoichiometry. Comput Mater Sci 2014;81:617–29.
[57] Yang Wenchao, Shen Weiwei, Zhang Ruirong, Cao Kaili, Zhang Jun, Liu Lin. Enhanced age-hardening by synergistic strengthening from MgSi and MgZn precipitates in Al-Mg-Si alloy with Zn addition. Mater Char 2020;169:110579. https://doi.org/10.1016/j.matchar.2020.110579. ISSN 1044-5803.
[58] Saito Takeshi, Flemming J, Ehlers H, Williams Lefebvre, Hernandez-Maldonado David, Bjørge Ruben, et al. Cu atoms suppress misfit dislocations at the β″/Al interface in Al–Mg–Si alloys. Scripta Mater 2016;110:6–9.
[59] Ding XP, Cui H, Zhang JX, Li HX, Guo MX, Lin Z, et al. The effect of Zn on the age hardening response in an Al–Mg–Si alloy. Mater Des 2015;65:1229–35. https://doi.org/10.1016/j.matdes.2014.09.086. ISSN 0261-3069.
[60] Yang Wenchao, Wang Mingpu, Zhang Ruirong, Zhang Qian, Sheng Xiaofei. The diffraction patterns from β″ precipitates in 12 orientations in Al–Mg–Si alloy. Scripta Mater 2010;62:705–8.
[61] ud Din Shamas, Kamram Z, Tariq NH, Hasan BA, petrov RH, bliznuk V, et al. The synergistic effect of Li addition on microstructure, texture, and mechanical properties of extruded Al-Mg-Si alloys. Mater Chem Phys 2016;xxx:1–12.
[62] ud Din Shamas, Kamran Javed, Hasan BA, Tariq NH, Mehmood M, Shamas uz Zuha M. Effect of thermo mechanical treatments and aging parameters on mechanical properties of Al–Mg–Si alloy containing 3wt.% Li. Materials & Design 2014;64:366–73. https://doi.org/10.1016/j.matdes.2014.07.062.
[63] Murayama M, Hono K. Pre-precipitate clusters and precipitation processes in Al–Mg–Si alloys. Acta Mater 1999;47:1537–48.
[64] Marioara CD, Andersen SJ, Stene TN, Hasting H, Walmsley J, van Helvoort ATJ, et al. The effect of Cu on precipitation in Al-Mg-Si alloys. Phil Mag 2007;87:3385–413. https://doi.org/10.1080/14786430701287377.
[65] Torster M, Ehlers FJH, Marioara CD, Andersen SJ, Holmestad R. Applying precipitate-host lattice coherency for compositional determination of precipitates in Al-Mg-Si-Cu alloys. Phil Mag 2012;92:3833–56. https://doi.org/10.1080/14786435.2012.693214.
[66] Cayron C, Sagalowicz L, Sagalowicz L, Buffat PA. Structural phase transition in Al-Cu-Mg-Si alloys by transmission electron microscopy study on an Al-4 wt% Cu-1 wt% Mg-Ag alloy reinforced by SiC particles. Philos Mag A: Physics of Condensed Matter, Structure, Defects and Mechanical Properties 1999;79:2833–51. https://doi.org/10.1080/01418619908212027.
[67] Matsuda Kenji, Ikeno Susumu. Yasuhiro Uetani & Tatsuo Sato metastable phases in an Al-Mg-Si alloy containing copper metallurgical and materials transactions A, vol. 32; 2001. p. 1293–9.
[68] Chakrabarti DJ, Laughlin David E. Phase relations and precipitation in Al–Mg–Si alloys with Cu additions. Prog Mater Sci 2004;49:389–410.
[69] Pan RK, Ma L, Bian N, Wang MH, Li PB, Tang BY, et al. First-principles study on the elastic properties of B′ and Q phase in Al-Mg-Si (-Cu) alloys. Phys Scripta 2013;87. https://doi.org/10.1088/0031-8949/87/01/015601.
[70] Marioara CD, Andersen SJ, Røyset J, Reiso O, Gulbrandsen-Dahl S, Nicolaisen TE, et al. Improving thermal stability in Cu-containing Al-Mg-Si alloys by precipitate optimization. Metall Mater Trans A Phys Metall Mater Sci 2014;45:2938–49. https://doi.org/10.1007/s11661-014-2250-0.
[71] Buchanan K, Colas K, Ribis J, Lopez A, Garnier J. Analysis of the metastable precipitates in peak-hardness aged Al-Mg-Si(-Cu) alloys with differing Si contents. Acta Mater 2017;132:209–21.
[72] Jia Z, Ding L, Cao L, Sanders R, Li S, Liu Q. The influence of composition on the clustering and precipitation behavior of Al-Mg-Si-Cu alloys. Metall Mater Trans A Phys Metall Mater Sci 2017;48:459–73. https://doi.org/10.1007/s11661-016-3850-7.
[73] Arnberg Lars, Aurivilluis Bengt. The crystal structure of $Al_xCu_2Mg_{12-x}Si_7$. Acta Chem Scand 1980;34:1–5.
[74] Takeshi Saitoa , Calin D. Marioarab , Sigmund J. Andersenb , Williams Lefebvrec and Randi Holmestada, Aberration-corrected HAADF-STEM investigations of precipitate structures in Al–Mg–Si alloys with low Cu additions. Phil Mag, 94:5, 520-531, DOI: 10.1080/14786435.2013.857051.
[75] Gazizova Marat, Daniel Marioara Calin, Jesper Friis, Wenner Sigurd, Holmesta Randi, Kaibyshev Rustam. Precipitation behavior in an Al–Cu–Mg–Si alloy during ageing. Mater Sci Eng, A 2019;767:138369.
[76] Saito T, Muraishi S, Marioara CD, Anderson SJ, Røyset J, Holmestad R. The Effects of Low Cu Additions and Predeformation on the Precipitation in a 6060 Al-Mg-Si Alloy. Metall Mater Trans A 2013;44:4124–35. https://doi.org/10.1007/s11661-013-1754-3.
[77] Saito T, Marioara CD, Andersen SJ, Lefebvre W, Holmestad R. Structural investigation of precipitates with Cu and Zn atomic columns in Al-Mg-Si alloys by aberration-corrected HAADF-STEM. In: J phys conf ser. Institute of Physics Publishing; 2014. https://doi.org/10.1088/1742-6596/522/1/012030.

[78] Saito T, Wenner S, Osmundsen E, Marioara CD, Andersen SJ, Røyset J, et al. The effect of Zn on precipitation in Al-Mg-Si alloys. Phil Mag 2014;94:2410–25. https://doi.org/10.1080/14786435.2014.913819.
[79] Ding L, Jia Z, Nie JF, Weng Y, Cao L, Chen H, et al. The structural and compositional evolution of precipitates in Al-Mg-Si-Cu alloy. Acta Mater 2018;145:437–50. https://doi.org/10.1016/j.actamat.2017.12.036.
[80] Andersen SJ, Marioara CD, Friis J, Bjørge R, Du Q, Ringdalen IG, et al. Directionality and column arrangement principles of precipitates in Al-Mg-Si-(Cu) and Al-Mg-Cu linked to line defect in Al. In: Materials science forum. Trans Tech Publications Ltd; 2017. p. 461–70. https://doi.org/10.4028/www.scientific.net/MSF.877.461.
[81] Saito T, Ehlers FJH, Lefebvre W, Hernandez-Maldonado D, Bjørge R, Marioara CD, et al. Cu atoms suppress misfit dislocations at the β″/Al interface in Al-Mg-Si alloys. Scripta Mater 2016;110:6–9. https://doi.org/10.1016/j.scriptamat.2015.07.033.
[82] Li K, Béché A, Song M, Sha G, Lu X, Zhang K, et al. Atomistic structure of Cu-containing β″ precipitates in an Al-Mg-Si-Cu alloy. Scripta Mater 2014;75:86–9. https://doi.org/10.1016/j.scriptamat.2013.11.030.
[83] Mørtsell Eva A, Marioara Calin D, Andersen Sigmund J, Ringdalen Inga G, Friis Jesper, Wenner Sigurd, et al. The effects and behaviour of Li and Cu alloying agents in lean Al-Mg-Si alloys. J Alloys Compd 2017;699. https://doi.org/10.1016/j.jallcom.2016.12.273.
[84] Cui Min, Jo Yong Hee, Haider Kayani Saif, Kim Hyoung-Wook, Lee Je-Hyun. Effects of Cu additions on the precipitation activation energy and mechanical properties of prestrained Al–Mg–Si alloys. J Mater Res Technol 2022;20:2629–37.
[85] Liu Xu, Ma Yin-Long, Wang Xuan, Zhang Shao-You, Zhang Ming-Xue, Wang Hui-Yuan. Enhanced long-term thermal stability and mechanical properties of twin-roll cast Al–Mg–Si alloys with Mn and Cu additions. Mater Sci Eng, A 2023:872. https://doi.org/10.1016/j.msea.2023.144945.
[86] Zang R, Ning Y, Ding L, Jia Z, Xiang K, Liu Q, et al. Study on properties and precipitation behaviour of 6000 series alloys with high Mg/Si ratios and Cu contents. Mater Char 2022;194. https://doi.org/10.1016/j.matchar.2022.112402.
[87] Sunde Jonas K, Lu Feng, Marioara Calin D, Holmedal Bjφrn, Holmestad Randi. Linking mechanical properties to precipitate microstructure in three Al-Mg-Si(-Cu) alloys. Mater Sci Eng 2021;807:140862.
[88] Guo MX, Zhang XK, Zhang JS, Zhuang LZ. Effect of Zn addition on the precipitation behaviors of Al–Mg–Si–Cu alloys for automotive applications. J Mater Sci 2017;52:1390–404. https://doi.org/10.1007/s10853-016-0433-3.
[89] Ding XP, Cui H, Zhang JX, Li HX, Guo MX, Lin Z, et al. The effect of Zn on the age hardening response in an Al-Mg-Si alloy. Mater Des 2015;65:1229–35. https://doi.org/10.1016/j.matdes.2014.09.086.
[90] Berg LK, Gjonnes J, Hansen V, Li XZ, Knutson wedel M, Waterlod G, et al. GP Zones in Al-Zn-Mg alloys and their role in artificial aging. Acta Mater 2001;49:3443–51.
[91] Wang Dongtao, Liu Shichao, Zhang Xiaozu, Li Xinzhong, Zhang Haitao, Nagaumi Hiromi. Fast aging strengthening by hybrid precipitates in high pressure die-cast Al-Si-Cu-Mg-Zn alloy. Material characterization 2021;179.
[92] Jiao NN, Lai YX, Chen SL, Gao P, Chen JH. Atomic-scale roles of Zn element in age-hardened AlMgSiZn alloys. J Mater Sci Technol 2021;70:105–12. https://doi.org/10.1016/j.jmst.2020.09.009. ISSN 1005-0302.
[93] Tian Aq, Xu Xh, Sun L, et al. Effects of interrupted ageing and asymmetric rolling on microstructures, mechanical properties, and intergranular corrosion behavior of Al-Mg-Si-Zn alloy. J. Cent. South Univ. 2022;29:821–35. https://doi.org/10.1007/s11771-022-4967-z.
[94] Ninive PH, Strandlie A, Gulbrandsen-Dahl S, Lefebvre W, Marioara CD, Andersen SJ, et al. Detailed atomistic insight into the β″ phase in Al-Mg-Si alloys. Acta Mater 2014;69:126–34. https://doi.org/10.1016/j.actamat.2014.01.052.
[95] Yang W, Wang M, Jia Y, Zhang R. Studies of orientations of β'' precipitates in Al-Mg-Si-(Cu) alloys by electron diffraction and transition matrix analysis. Metall Mater Trans A Phys Metall Mater Sci 2011;42:2917–29. https://doi.org/10.1007/s11661-011-0680-5.
[96] Ding Lipeng, Jia Zhihong, Zhang Zhiqing, Sanders Robert E, Liu Qing, Yang Guang. The natural aging and precipitation hardening behaviour of Al-Mg-Si-Cu alloys with different Mg/Si ratios and Cu additions. Mater Sci Eng 2015;A627:119–26.
[97] Kim JH, Kobayashi E, Sato T. Effects of Cu addition on behavior of nanoclusters during multi-step aging in Al-Mg-Si alloys. Mater Trans 2011:906–13. https://doi.org/10.2320/matertrans.L-MZ201121.
[98] Weng Yaoyao, Jia Zhihong, Ding Lipeng, Pan Yanfeng, Liu Yingying, Liu Qing. Effect of Ag and Cu additions on natural aging and precipitation hardening behavior in Al-Mg-Si alloys. J Alloys Compd 2017;695:2444–52.
[99] Ali AM, Gaber AF, Matsuda K, Ikeno S. The structure and kinetics of the nanoscale precipitation processes in Al-1.0 wt pct Mg2Si-0.4 wt pct Mg-0.5 wt pct Ag alloy. Metall Mater Trans A Phys Metall Mater Sci 2013;44:5234–40. https://doi.org/10.1007/s11661-013-1862-0.
[100] Zhang H, Zheng Z, Lin Y, Luo X, Zhong J. Effects of Ag addition on the microstructure and thermal stability of 6156 alloy. J Mater Sci 2012;47:4101–9. https://doi.org/10.1007/s10853-012-6264-y.
[101] Weng Yaoyao, Jia Zhihong, Ding Lipeng, Muraishi Shinji, Liu Qing. Clustering behavior during natural aging and artificial aging in Al-Mg-Si alloys with different Ag and Cu addition. Mater Sci Eng, A 2018;732:273–83.
[102] Weng Yaoyao, Ding Lipeng, Zhang Zezhong, Jia Zhihong, Wen Boyang, Liu Yingying, et al. Effect of Ag addition on the precipitation evolution and interfacial segregation for Al-Mg-Si alloy. Acta Mater 2019;180:301–16.
[103] Djema Oussama, Bouabdallah Mabrouk, Badji Riad, Saadi Amr, Kherrouba Nabil, Sahli Amane. Isothermal and non-isothermal precipitation kinetics in Al–Mg–Si-(Ag) alloy. Mater Chem Phys 2020;240:122073. https://doi.org/10.1016/j.matchemphys.2019.122073. ISSN 0254-0584.
[104] Banhart J, Lay MDH, Chang CST, Hill AJ. Kinetics of natural aging in Al-Mg-Si alloys studied by positron annihilation lifetime spectroscopy. Phys Rev B 2011;ume-83. https://link.aps.org/doi/10.1103/PhysRevB.83.014101.
[105] Raabe D, Tasan CC, Olivetti EA. Strategies for improving the sustainability of structural metals. Nature 2019;575:64–74. https://doi.org/10.1038/s41586-019-1702-5.
[106] Kotadia HR, Qian M, Das A. Microstructural modification of recycled aluminium alloys by high-intensity ultrasonication: observations from custom Al–2Si–2Mg–1.2Fe–(0.5,1.0)Mn alloys. J Alloys Compd 2020;823. https://doi.org/10.1016/j.jallcom.2020.153833.
[107] Ostermann F. Anwendungstechnologie aluminium. Springer Berlin Heidelberg; 2014. https://doi.org/10.1007/978-3-662-43807-7.
[108] Granta Design Limited. CES EduPack software. Granta Des Ltd; 2009.
[109] Raabe D, Ponge D, Uggowitzer PJ, Roscher M, Paolantonio M, Liu C, et al. Making sustainable aluminum by recycling scrap: The science of "dirty" alloys. Prog Mater Sci

2022;128:100947. https://doi.org/10.1016/j.pmatsci.2022.100947. ISSN 0079-6425.
[110] Pereira LH, Asato GH, Otani LB, Jorge AM, Kiminami CS, Bolfarini C, et al. Changing the solidification sequence and the morphology of iron-containing intermetallic phases in AA6061 aluminum alloy processed by spray forming. Mater Char 2018;145:507–15. https://doi.org/10.1016/j.matchar.2018.09.006.
[111] Paraskevas D, Ingarao G, Deng Y, Duflou JR, Pontikes Y, Blanpain B. Evaluating the material resource efficiency of secondary aluminium production: a Monte Carlo-based decision-support tool. J Clean Prod 2019;215:488–96. https://doi.org/10.1016/j.jclepro.2019.01.097.
[112] Wagner Fabrice, Bollmann Christian, Brüggemann Thiemo, Hojda Stephan, Teller Marco, Hirt Gerhard. Model framework for the simulation of microstructure and yield stress during aging of industrial Al-Mg-Si aluminum alloys. Procedia Manuf 2020;50:Page368–375.
[113] Zhang Mingshan, Wang Junsheng, Han Jiaqiang, Sui Huaiming, Huang Houbing, Jin Ke, et al. Optimization of heat treatment process of Al-Mg-Si cast alloys with Zn additions by simulation and experimental investigations. Calphad 2019;67:101684.
[114] Myhr OR, Grong Ø, Andersen SJ. Modelling of the age hardening behaviour of Al–Mg–Si alloys. Acta Mater 2001;49(1):65–75.
[115] Myhr O, Grong Ø, Schäfer C. An extended age-hardening model for Al-Mg-Si alloys incorporating the Room-temperature storage and cold deformation process stages. Metall Mater Trans A 2015;46(12):6018–39.
[116] MatCalc software package for computer simulation of phase transformation and microstructure evolution in metallic systems.
[117] Schmid F, Dumitraschkewitz P, Kremmer T, Uggowitzer PJ, Tosone R, Pogatscher S. Enhanced aging kinetics in Al-Mg-Si alloys by up-quenching. Commun Mater 2021;2:58. https://doi.org/10.1038/s43246-021-00164-9.
[118] Fischer FD, Svoboda J, Appel F, Kozeschnik E. Modeling of excess vacancy annihilation at different types of sinks. Acta Mater 2011;59:3463–72.
[119] Qiang D, Kai T, Marioar CD, Sigmund JA, Bjørn H, Randi H. Modeling over-ageing in Al-Mg-Si alloys by a multi-phase CALPHAD– coupled Kampmann–Wagner numerical model. Acta Mater 2017;122:178–86.
[120] Bardel D, Perez M, Nelias D, Deschamps A, Hutchinson CR, Maisonnette D. .Coupled precipitation and yield strength modelling for non-isothermal treatments of a 6061-aluminium alloy. Acta Mater 2014;62:129–40.
[121] Zhang Y, Li H, Li Z, Mariusz B, Senkara J. Quantitative analysis of the solute redistribution and precipitate of Al-Mg-Si series alloys resistance spot welds after post-weld heat treatment. JMRT 2021:5906–19.
[122] Poon I, Marceau RKW, Xia J, Liao XZ, Ringer SP. Precipitation processes in Al-Cu-Mg-Sn and Al-Cu-Mg-Sn-Ag. Mater Des 2016;96:385–91. https://doi.org/10.1016/j.matdes.2016.02.048.